3D Modelling of Excavation-Induced Anisotropic Responses of Deep Drifts at the Meuse/Haute-Marne URL

Mountaka Souley, Minh-Ngoc Vu, Gilles Armand

3D modelling of excavation induced anisotropic responses of deep drifts at the Meuse/Haute-Marne URL

Mountaka Souley[1,*], Minh-Ngoc Vu[2], Gilles Armand[2]

[1] Ineris, Ecole des Mines, Campus ARTEM, 54042 Nancy, France ([*] Corresponding author: Mountaka.Souley@ineris.fr)
[2] Andra R&D, 92298 Chatenay-Malabry, France

Abstract

Understanding the excavation induced fractured zone (EFZ) around drifts is paramount in the context of the deep geological disposal for nuclear waste since fractures can introduce pathways for the migration of radionuclides. Drifts in the Meuse/Haute-Marne Underground Research Laboratory (URL) have been essentially excavated following the two main directions of major and minor horizontal stresses. Field observations on the two drifts GCS (parallel to major horizontal stress direction) and GED (parallel to minor horizontal stress direction) in the URL show anisotropic shapes of EFZ around drifts through both orientations and anisotropic convergences. These anisotropic responses resulted from the inherent and/or induced anisotropies of the host rock; as well as the anisotropic stress field.

This study focuses on 3D numerical modelling of excavation induced anisotropic responses including shape and extent of EFZ, and short term convergences of drifts. The main assumption is that the failure of claystone material is due to fracturing along weakness planes (ubiquitous joints) and the failure of the rock matrix. The ubiquitous joint failure is represented by perfectly plastic models for both tensile and shear yield functions. Their orientation is determined from the stress state based on the fracture mechanics, which includes tensile, longitudinal splitting and shear (conjugate planes) cracks. The rock matrix is assumed to be elastoplastic with hardening, softening and residual behaviours. Confining pressure dependency for the post-peak behaviour with a brittle-ductile transition is taken into account for the rock matrix. The proposed model is implemented into a commercial numerical software *FLAC^{3D}*. The main features of the implemented model are shown by the simulation of laboratory triaxial compression tests, as well as field observation within the URL. In particular, comparisons between 3D simulations of GCS and GED drifts with in situ observations shows promising results, which demonstrates advances of present model advances with respect to existing models.

Keywords: Callovo-Oxfordian claystone; Weakness planes; 3D simulation; excavation-induced damage zone; induced anisotropy; short-term behaviour.

1. Introduction

The Callovo-Oxfordian claystone (COx) is considered as a potential geological host formation for high-level and intermediate-level long-lived radioactive waste in France since this geological formation exhibits in their natural state very favourable conditions for long term confining of nuclear waste. In 2000, the French National Radioactive Waste Management Agency (Andra) started building an Underground Research Laboratory (URL) in

Meuse/Haute-Marne in order to demonstrate the feasibility of constructing and operating a reversible deep geological disposal in COx formation (see Fig. 1). The excavation of galleries at the main level (490 m depth) of the URL has been essentially performed through the direction of the major and minor horizontal principal stresses. The major horizontal stress $\sigma_H \approx 16$ MPa, while the minor horizontal stress σ_h is close to the vertical stress σ_v being equal to the overburden weight ($\sigma_v \approx \sigma_h \approx 12$ MPa) (Wileveau et al. 2007). From the analysis of field observation, Armand et al. (2014) showed that excavation induces fracture network around the drifts including shear and extensional fractures. Indeed, the authors have reported the existence of two adjacent zones around drifts: a "connected" fractured zone (ZFC) including both shear and tensile fractures, and a more extended "discrete" fractured zone (ZFD) including only the shear fractures. The ZFC close to the drift wall would correspond, in term of permeability, to the well-known EDZ (Excavation Damaged Zone) in which the permeability increases significantly (Tsang et al. 2005). Whereas, the ZFD located between the EDZ and the intact rock mass would represent the EdZ (Excavation Disturbed Zone) with a moderate permeability change. The in situ observations show an anisotropic extent of the induced fractured zone even for the drifts parallel to major horizontal stress for which, the initial total stress is almost isotropic in the drift section. Anisotropies in convergence and pore pressure distribution have been also evidenced by field measurements (Armand et al. 2013, 2015, 2017b, c; Vu et al. 2020a, b). Different factors contribute probably to this anisotropic response of the COx due to the excavation such as: anisotropy of far field stresses; inherent anisotropy of rock matrix or/and induced anisotropic responses. Indeed, the laboratory tests performed on the COx samples show a slight inherent anisotropy of the stiffness and strength (Zhang et al. 2012; Armand et al. 2017a, b; Zhang et al. 2019). It is observed that the maximum strength is reached in parallel and normal to the bedding, while the lowest strength occurs at the load orientation in the range of 30°-60° with respect to the bedding. Regarding the stiffness, Young's modulus in the direction parallel to the bedding planes is higher than that in the perpendicular direction. The ratio between them varies from 1.2 to 2. Moreover, the induced fractures provoke an "induced anisotropy" in the rock mass. For instance, anisotropic distribution in pore pressure is attributed to both elastic anisotropy and induced fracture zone (Armand et al. 2017b, c; Vu et al. 2020b).

The induced fracture zones around drifts in URL have been of interest for several numerical studies. Particularly, a benchmark exercise has been proposed in order to provide an overall view of the developed and used models regarding the field observations (Seyedi et al. 2017). Modelling based on both discrete elements (Yao et al. 2017) and continuum mechanics (Manica et al. 2017; Pardoen et al. 2015; Pardoen and Collin 2017; Souley et al. 2017; Trivellato et al. 2019) approaches has been considered. However, inherent anisotropy is usually necessary to model the anisotropic shapes of EFZ, as well as the anisotropy in convergences for the gallery GCS ($//\sigma_H$). Moreover, they usually need the hydro-mechanical coupling and advanced numerical models to improve the results, such as non-local model (Manica et al. 2018; Manica et al. 2021a, b), second gradient regularization (Pardoen and Collin 2017), phase field model (Yu et al. 2021a, b). However, the modelling of anisotropic responses around drifts within URL is still challenging. Indeed, previous studies have considered the tunnel excavation by assuming plane strain conditions (2D assumption) with the convergence-confining method. This assumption is not suitable for the 3D configuration within the URL or the future radioactive waste disposal (Cigéo), for instance, the intersection between drifts. Moreover, the reproduction of major observations for drifts excavated following both orientations

of major and minor horizontal principal stresses (i.e. GCS and GED) with a unique set of parameters is still a challenge.

This study aims at proposing a phenomenological macroscopic model for modelling in 3D the induced anisotropies of short-term behaviour of the COx claystone due to the excavation. Both drifts GCS and GED are considered, and the comparison with the in situ observations in terms of EFZ and convergences is made. The rock fracturing is modelled by a coupling between weakness planes and elastoplastic rock matrix. The phenomenological model proposed by Souley et al. (2011) is improved to describe the behaviour of the rock matrix. It is an elasto-plastic model, in which the elasticity is linear and transversely isotropic, and the plasticity is formulated from a generalization Hoek and Brown criterion for shear behaviour and Rankine criterion in tension. Non-associated flow rule is used for shear plasticity, while associated flow rule is assumed in tension. This constitutive model describes the behaviour of COx observed by tests on the sample, including strain hardening, strain softening and residual phases, as well as the transition between the brittle failure at low confining pressure and the ductile behaviour under high confining stresses. Weakness planes concept (commonly called "Discontinuous weakness plane" or "Ubquituous Joints") is introduced to model the failure of bedding planes and the induced anisotropy within large-scale continuum approaches. Nevertheless, no weakness plane is predefined. Joints occur according to the stress state and their orientation is determined based on the fracture mechanic theory. There are three fracture types (Paterson 1978; Diederichs 2003, 2007; Jaeger et al. 2007): tensile crack perpendicular to the tensile stress direction; longitudinal splitting crack when the confining stress is equal or close to zero and crack occurring following two conjugate planes similar to those observed in the triaxial compression tests under moderate confining pressure. An elastic perfectly plastic behaviour based on the Mohr-Coulomb and Rankine criteria is used to describe the shear and tensile failures along the weakness planes. The main feature of the proposed model will be firstly illustrated by the simulation of a triaxial test. Secondly, the model is applied for 3D modelling of excavation of two drifts in the URL (GCS//σ_H and GED//σ_h). 3D simulation allows to overcome the convergence-deconfining assumption and gives 3D characteristics of the results (convergence and EFZ change from one section to another). The EFZ is carefully analysed and compared to the field observation, particularly their extent. Comparisons are also made for short term convergences between the numerical solution and the analysis of in-situ measurements conducted by Armand et al. (2013) and an empirical model proposed by Guayacan Carrillo et al. (2016b).

This paper is organised as follows. Section 2 gives an overview on major experimental observations and constitutive models of anisotropic behaviour of geomaterials. Section 3 shows the constitutive equations of the present model and its main features through the simulation of triaxial compression tests. Section 4 presents the 3D modelling of two drifts in the URL and the comparison between the numerical results to the field measurements. Conclusions and perspectives will be finally drawn in section 5.

2. Review of the anisotropic behaviour of geomaterials

2.1. Experimental observations

In regards with their microstructure such as particle arrangement, micro cracks, bedding (weakness) planes, among others, rocks exhibit often anisotropic behaviour (deformation and strength). Considerable efforts have been devoted to the study the rock anisotropy. Much research had been carried out, including experimental characterization (Nova 1980; Niandou et al. 1997; Duveau et al. 1998; Tien et al. 2006; Nasseri et al 2003; Shengli et al. 2012, Abdi et al. 2014; Zhang et al. 2019; etc.), theoretical studies and numerical modelling (Duveau and Shao 1998; Pietruszczak et al. 2002; etc). All the results obtained have shown that the rock strength varies with the loading orientation. The variation of the compressive strength versus the angle between the loading orientation to a reference direction (e.g. bedding plane) is the most common representation of the nature of strength anisotropy. Indeed, the strength of bedded rock usually depends on the stress state and the loading orientation to the stratification. The maximum strength is often found in the directions normal and parallel to the bedding and the minimum strength is usually reached when the angle of inclination between the major stress and the weak planes is ranged from 30 to 60°. The ratio of resistance in the two main directions related to the anisotropy or the ratio between the minor and major strengths are used to quantify the degree of anisotropy. Failure may occur in very complex ways, combining sliding and separation along the planes of weakness, and a shear band in the matrix. This constitutes one of the main ingredients of the macroscopic phenomenological model proposed subsequently.

Measurement of the propagation velocities of ultrasonic waves on Callovo Oxfordian claystone showed a structural anisotropy (David et al. 2005). The anisotropy of the wave propagation speed and the dynamic modules has been also observed on the laboratory tests with acoustic emissions monitoring (Sarout and Guéguen 2008). These tests show a ratio of dynamic elastic modulus in the parallel direction and that in the perpendicular direction to the bedding from 1.05 to 1.4. The measurement from triaxial compression tests show that this elastic anisotropy ratio could be larger but remains lower than 2 (Zhang et al. 2012; Zhang et al. 2019). Besides, test results showed that the strengths in the directions parallel and perpendicular to the stratification are close. The lowest strength is measured at about 30°- 45° with respect to the bedding plane. The ratio between minimum and maximum strength values is close to 0.7 for most of the performed tests (Zhang et al. 2019).

Compared to Opalinus clay and Tournemire shale, the shear strength is slightly greater in the direction parallel to the bedding compared to that in the perpendicular direction. In addition, the minimum strength is reached for samples at 45 ° for Opalinus clay, while for Tournemire shale, this minimum is reached between 30 and 60°.

Concerning the mechanical anisotropy characterized by the ratio of the elastic deformability normal and parallel to bedding, in comparison with the Opalinus clay and the Tournemire shale, the anisotropy of the COx claystone is less pronounced. In addition, the elastic stiffness of the COx claystone is higher than that of the Opalinus clay but lower than the Tournemire shale (Zhang et al. 2019).

2.2. Modelling approaches

Based on the experimental results, various failure criteria for anisotropic materials exhibiting a visible inherent anisotropy have been proposed in the literature. Subsequently, these criteria led to the development of anisotropic rheological models in the framework of damage mechanics and/or plasticity.

(a) Theoretical criteria

The rock is viewed as a solid body with properties that continuously vary with the load direction. The main features of these mathematical criteria are that anisotropy orientation issues are explicitly considered, and their formulations mostly use linear and quadratic terms of the stress components. Pariseau (1979) developed a failure theory for anisotropic rocks by modifying the orthotropic criterion of Hill (1950) for metals built in the framework of plasticity. Pariseau's theory takes into account the failure of geomaterials under hydrostatic stress, the difference between compressive and tensile loadings, the dependence of the strength on the mean stress (or confining stress), but also predicts a continuous variation of strength as a function of the orientation to the bedding. The approach of Boehler and Sawczuk (1977) is more general and rigorous for transverse isotropic and orthotropic materials and based on the generalisation of Mohr-Coulomb and von Mises isotropic criteria within the framework of non-linear mechanics of anisotropic solids and tensor functions theory. Even if for the criteria of this group, the thermodynamic framework is well-stated, it is often difficult to identify the involved parameters from conventional laboratory tests. This, in addition to their mathematical complexity and lack of their experimental validation, limits their applications to engineering practices (Mróz and Maciejewski 2003, Lee and Pietruszczak 2008).

(b) Empirical criteria

The empirical criteria are mainly extensions of isotropic criteria (Coulomb, Hoek and Brown or von Mises widely used in engineering) and based on the theory of variational strength parameters (i.e. cohesion c and friction ϕ for Mohr-Coulomb or von Mises criteria; or parameters m, s and σ_c for Hoek and Brown criterion) as a function of the angle between the load direction and the bedding. These empirical criteria are based on the concept of the critical plane which corresponds to the plane in stresses space in which the rock damage or failure reaches its maximum value. Initiated by Coulomb, the failure function is defined in terms of tensile components acting on the physical plane of failure; that is to say, a potential failure plane corresponding to a maximum of failure condition (Walsh and Brace 1964; Jaeger and Cook 1979; Hoek and Brown 1980; Hoek 1983; Duveau and Shao 1998; Pouragha et al. 2018; etc). Even if they suffer from physical and mathematical fundamentals, empirical criteria are of interest in engineering because they simply extend isotropic criteria widely used in numerous applications and the identification of the involved directional parameters can be achieved easily by fitting experimental data (McLamore and Gray 1967; Nasseri et al. 2003; Lee and Pietruszczak 2008; Saroglou and Tsiambaos 2008; Abdi et al. 2014; Wang and Yu 2014).

(c) Criteria based on the fabric tensor

In addition to the phenomenological approach to model the failure of anisotropic geomaterials through the strength characteristics presented above for the empirical criteria, other researchers have introduced a fabric tensor concept

to describe the bedding structure of geomaterials (Pietruszczak and Mróz 2000, 2001; Lee and Pietruszczak 2008). Then, an anisotropic strength theory relating the microstructure was then developed by these authors. In this approach, the critical plane incorporating the spatial distribution of microcracks was applied for a quantitative description of compressive strength variation with the loading orientation relative to the anisotropy axes (Mróz and Maciejewski 2002, 2003). Since then, several anisotropic criteria based on this approach have been proposed by extending the Coulomb, Lade or Hoek and Brown criteria for the maximum strength acting on the microcrack or critical planes (Lade 2007, Lee and Pietruszczak 2008). One of the advantages of the fabric tensor approach is that the anisotropic failure and mechanical behaviour could comprehensively reflect the structural and mechanical effects of the bedding structure from microstructural observations, and the theoretical framework is thermodynamically well established. In addition, its numerical implementation is relatively easy (Pardoen et al. 2015, Nguyen and Le 2015), which facilitates their use in engineering and research applications.

(d) Criteria based on the concept of "Ubiquitous Joints" or "Discontinuous Weakness planes"

These criteria, part of a discontinuous approach, are based on the weakness or critical planes (Sainsbury et al. 2008, Tran-Manh et al. 2015; Ismael and Konietzky 2019) and well suited for rocks and geomaterials with visible inherent anisotropy. In these criteria, the failure mechanisms that occur along the weakness planes and the intact rock are distinguished. The basic assumption is that the rock fails either through shear and tensile fractures or sliding along weak planes and these different failure modes are used together to determine the actual failure criterion. Assuming that the weakness planes are oriented along the cracks and based on the extension of Griffith's theory, several criteria within this category were proposed in the literature (Walsh and Brace 1964; Hoek and Brown 1980, Hoek 1983; Duveau and Shao 1998). Generally speaking, the rock matrix is modelled by nonlinear criteria involving the three invariants of stresses, while sliding along the planes of weakness follows the Mohr-Coulomb criterion, Hoek and Brown criterion or the JRC-JCS model (Bandis et al. 1985) developed for rock fractures (Wang and Huang 2009; Prassetyo et al. 2017).

As for the empirical criteria, most of the criteria within this category are straightforwardly used in rock engineering, because they are stated on well-familiar strength criteria. Finally, beyond its interest to model the failure of anisotropic rocks, the discontinuous approach can also be interesting for modelling the induced damage by combining the isotropy or inherent anisotropy of the rock with its cracking by relating the orientation of the induced fracture planes to that of the loading, as discussed later in the proposed constitutive model.

(e) Constitutive models

Based on the previous 4 groups of anisotropic criteria, several anisotropic mechanical models have been developed within the framework of continuum damage mechanics and/or plasticity, according to two main approaches: micromechanical and phenomenological.

The micromechanical approach allows to accurately account for the certain physical mechanisms involved in the nucleation and the propagation of microcracks on a suitable micro-structural scale. The evolution of the damage variable is based on an analysis of the effective mechanical properties of the microcracks: the criterion of

nucleation and microcracks growth being evaluated at the microscopic scale. The bases of the micromechanical models are the kinetics of microcracks, the growth criterion, as well as the evaluation of elastic properties due to displacements through discontinuities at the microcrack scale. Thus, these models are formulated in a rigorous micro-macro framework following a general homogenization procedure of heterogeneous media, as well as clear thermodynamic considerations of irreversible mechanisms of dissipation (Zhu and Shao 2017) and applied to structural calculations (Levasseur et al. 2015). Other micromechanical models use the fabric tensor concept for induced anisotropy of initially anisotropic material and consider the directional variation in the evaluation of microcracks strength (Shen and Shao 2015, Levasseur et al. 2015). The numerical implementation of micromechanical models is rather laborious, even though progress has been made in recent years in terms of computing resources, resolution algorithms and homogenization techniques. It is therefore not surprising nowadays to find engineering applications of these models in the literature: this is the case for Tournermire claystone (Pietruszczak et al. 2002, Nguyen and Le 2015) and COx claystone (Pardoen et al. 2015) and Opalinus clay (Nguyen and Le 2015).

Phenomenological models are based on the reproduction of observed phenomena (damage and/or plasticity) from mechanical tests performed in the laboratory or in situ. They are stated on the theory of damage and plasticity of the homogeneous continuous medium using internal variables (scalar, vector, tensor type) to describe the involved mechanisms. The evolution of damage and plastic internal variables is then formulated according to the stress or strain tensors as part of the thermodynamics of irreversible processes and/or the linear fracture mechanics for damage. The elastoplastic models formulated on the concept of ubiquitous joints are fully part of this category. The phenomenological models provide a powerful tool that can be easily implemented in numerical codes. However, they have the disadvantage of employing some concepts or assumptions driven by mathematical conveniences rather than physical interpretations of microcracking processes such as the concept of effective stresses, the unilateral effect of microcrack reclosure or the coupling between damage and plasticity.

Several phenomenological models are reported in the literature and numerous have been used to describe the mechanical and hydromechanical behaviour of COx claystone, without however reproducing entirely the observations (convergences, pore pressure, expansion, shape and extension of the fractured zones) carried out around the URL drifts oriented in the two directions of the horizontal principal stresses. This is one of the reasons why we propose a phenomenological model for the behaviour of COx claystone. More specifically, unlike all models based on the concept of ubiquitous joints published in the literature (Wang and Huang 2009, 2014; Tran-Manh et al. 2015; Prassetyo et al. 2017; Ismael and Konietzky 2017, 2019; Chang and Konietzky 2018) where the weakness or critical planes have a fixed orientation independently to the loading, herein the weakness plane is not necessarily imposed (which is well-suited for non-visible anisotropies) and the strength anisotropy is induced by these planes of weakness: this can be viewed as induced damage without changes in elastic stiffness.

3. Constitutive model equations

3.1. Main assumptions

As shown by Armand et al. (2017b), the main features of the short-term mechanical behaviour observed on claystone samples under triaxial tests can be summarized as follows: (a) the behaviour is linear elastic under low deviatoric stress; (b) strain hardening starts approximately at 50% of the peak strength; (c) strain softening for a confining pressure lower than 20 MPa; (d) the residual behaviour is completely frictional and governed by the behaviour of the induced well-localized shear bands or macro-cracks (Bésuelle and Lanata 2014; Desbois et al. 2017; Zhang 2016, Zhang et al. 2019). There is a strong dependence of the mechanical behaviour on the confining pressure, marked by a transition from a brittle failure toward a ductile behaviour when the confinement increases.

The basic assumption is that the failure of an anisotropic material is due to either fracturing of bedding planes (and/or induced weakness planes) and the failure of the rock matrix. Unlike models based on the concept of "ubiquitous joints" widely published in the literature (Wang and Huang 2009, 2014; Tran-Manh et al. 2015; Prassetyo et al. 2017; Ismael and Konietzky 2017, 2019; Chang and Konietzky 2018; among others) in which the orientation of weakness planes is imposed consistent for geomaterials with visible inherent anisotropy, herein no predefined weakness plane is assumed in advance. The critical plane is specified by maximizing the yield function with respect to the plane orientation (Walsh and Brace 1964; Jaeger and Cook 1979; Hoek and Brown 1980; Hoek 1983; Duveau and Shao 1998).

Experiments on brittle failure reveal two fundamental types of induced fractures: tensile/extension (mode I) and shear (modes II and III) which individually induces different displacement field with respect to the fracture surfaces and orientation of the fracture plane depending on the applied stress state. In Mode I, fractures are associated with either tensile fractures occurring when the maximum principal stress σ_3 (with the convention that compressive stresses are assumed to be negative and $\sigma_1 \leq \sigma_2 \leq \sigma_3$) reaches the tensile strength, for instance, under uniaxial tension or axial extension conditions in. This type of fracture also occurs when the major principal stress σ_3 (or confining pressure) is equal or close to zero and the minimum compressive stress σ_1 is axial stress, as in uniaxial compression configuration. This fracture is also called the longitudinal splitting one that its occurrence is evidenced by experimental observation from laboratory samples and in the vicinity of underground structures (Paterson 1978; Diederichs 2003; Jaeger et al. 2007), as well as by theoretical analysis (Diederichs 2007). The main characteristic of this type of fracture is a separation of two formerly contiguous surfaces with a displacement field parallel to the maximum principal stress σ_3 and normal to the fracture plane.

Under moderate confining pressure, shear failure occurs along two conjugates shear planes located symmetrically with respect to the direction of the axial stress σ_1 (Paterson 1978). The orientation of these fracture planes can then be determined based on the weakness plane model firstly introduced by Jaeger (1960) or on its generalization through the critical plane approach. The latter is based on the stresses acting on the plane where the crack nucleation is expected to occur (Jaeger and Cook 1979; Pietruszczak and Mróz 2001; Lee and Pietruszczak 2008; Pouragha et al. 2018). Finally, the main concept of the critical plane approach is to search for the orientation of a

critical plane on which the failure criterion reaches its maximum value. Then the critical plane framework requires finding the first stress state during loading history that satisfies the yield condition on a potential plane (Pouragha et al. 2018), for example the maximum of failure criterion (Walsh and Brace 1964; Jaeger and Cook 1979; Hoek and Brown 1980; Hoek 1983; Duveau and Shao 1998).

The straight-line approximation to the shear fracture envelope is known as the Coulomb fracture criterion for shear strength, whose slope represents the competing effects between normal and shear stresses (σ_n, τ) acting on these fractures. Since this shear strength line has a positive slope, the angle θ_f is then less than 45°. Considering the potential fracture planes for a given (σ_n, τ), the Coulomb-Navier criterion allows to determine the orientation of the conjugate shear planes with respect to σ_1–direction to be expressed as follows: $\theta_f = \pm\left(\frac{\pi}{4} - \frac{\varphi_{wp}}{2}\right)$ where φ_{wp} is the internal friction angle of the weak planes.

In addition, under triaxial compression test with sufficiently high confining pressure, the rock becomes fully ductile with the appearance of a network of shear micro-cracks accompanied by an amount of plastic deformation (Jaeger et al. 2007). These different fracture modes observed both on samples during laboratory tests and in situ in the vicinity of an opening are recalled in Fig. 2a (Diederichs 2003). Finally, under high confinements, an absence of scale effect on the rock strength with strength at laboratory-scale almost identical to that in situ.

Based on these experimental evidences of failure in the field of rock mechanics, the induced anisotropy is herein described by weak planes whose orientation depends on the induced stress distribution. More precisely we assume that: (a) extension fracture occurs in tension and the fracture is normal to the tensile stress direction; (b) splitting fracture when the principal stress σ_3 is equal or close to zero and fracture plane is perpendicular to σ_3 (i.e. parallel to σ_1-direction); (c) under triaxial compression configuration we consider that the rock fails along conjugate fractures with an angle θ_f about $\pm\left(\frac{\pi}{4} - \frac{\varphi_{wp}}{2}\right)$ with respect to the direction of σ_1. In the latter case, an evolution of θ_f from 0 (values of σ_3 near zero) to $\left(\frac{\pi}{4} - \frac{\varphi_{wp}}{2}\right)$ with the increase in confining pressure could be expected. However, in absence of experimental data on the value of confining stress from which the orientation of the induced fracture plane reaches $\left(\frac{\pi}{4} - \frac{\varphi_{wp}}{2}\right)$, a value of 0.1 MPa is assumed in this paper. Then, the induced macrocrack orientation (depending on the current stress state) adopted in this study, is schematically illustrated in Fig. 2b. This choice of the weakness plane orientation remains in accordance with the experimental results of failure plane orientation reported by Zhang (2016) and Bésuelle and Lanata (2014) as well as with theoretical analysis by Jaeger et al. (2007) and Diederichs (2003).

Thus, the main assumptions are summarized below. The matrix is assumed to be linear elastic, transversely isotropic (below the elastic limit) and plastic with strain hardening and softening followed by a residual stage. The tensile and shear plasticity are described by isotropic nonlinear yield functions derived from the laboratory characterization. A non-associated flow rule is used with the absence of volumetric strain beyond large plastic distortion in order to reproduce better the volumetric behaviour (mainly sliding) inside the induced shear bands or fracture planes. Induced fractures are modelled as the planes of weakness represented by joints whose orientations have been discussed above. A perfectly plastic behaviour is assumed along these weakness planes according to the

Mohr-Coulomb criterion for shear plasticity and Rankine criterion for tensile plasticity. The elasticity of the weakness plane is also considered to be linear and transversely isotropic.

There are no experimental data available on the anisotropic plastic behaviour of COx claystone regarding the elastic limit and the residual strength as a function of the bedding angle α (i.e angle between the axial load direction and the bedding, which coincides with the sampling orientation). As a first approximation, we do not consider the evolution of yield surfaces with respect to the bedding angle for the strain hardening/softening and residual phases. In other words, the matrix remains plastically isotropic. It is this same isotropic plasticity assumption that has been assumed for identifying the Hoek-Brown parameters for elastic limit, peak and residual strengths of COx claystone from laboratory data (Souley et al. 2011, Zhang and Rothfuchs 2004, Souley et al. 2017, Zhang 2016).

Regarding the COx claystone, triaxial tests with loading-unloading cycles performed before the peak strength do not indicate changes in elastic moduli (Zhang and Rothfuchs 2004, Zhang et al. 2019). This justifies our choice to limit the pre-peak phase to an elastoplastic mechanism with strain hardening. Conversely, the post-peak behaviour of COx claystone characterized through biaxial and triaxial tests by numerous authors is accompanied by the formation of well-localized shear bands or macroscopic cracks (Bésuelle and Lanata 2014; Desbois et al. 2017; Zhang 2016; Zhang et al. 2019). However, no quantification of strength, cohesion and modules decrease has been done in these shear bands or fractured samples during the post-peak regime. The damage of the COx claystone, which is then only observed in the post-peak phase, was approached in the proposed model by the theory of plasticity by assimilating these fractures or shear bands to critical planes of failure and which results in a loss of strength without a modification of the effective stiffness.

3.2. Case of the intact rock matrix

The rheological model proposed is based on results obtained from different laboratory characterizations on the mechanical behaviour of COx claystone (Armand et al. 2017b).

It has been shown that a failure criterion based on the Hoek and Brown (1980) criterion (eq. 1) is suitable for describing the shear strength of the COx claystone (Su 2003; Souley et al. 2011; Souley et al. 2017). However, since the COx claystone in its natural state have no tectonic fractures, classical signification of the Hoek and Brown parameters cannot be used for determining the rock mass strength from the results of tests on samples and taking into account the fracturing of the rock.

$$\sigma_1 = \sigma_3 - \sqrt{-m\sigma_c\sigma_3 + s{\sigma_c}^2} \qquad (1)$$

where σ_1 and σ_3 are minor and major principal stresses (compressive stresses are negative, $\sigma_1 \leq \sigma_2 \leq \sigma_3$), m and s are material constants, σ_c is the value of stress reached at the elastic limit and peak under unconfined compressive condition.

The generalization of equation (1) in the space of three stress invariants (p, q, θ) leads to the following criterion for plasticity initiation and peak strength:

$$F_s^{\,m} = \frac{4}{3}\frac{cos^2\theta}{A}q^2 + \left(\frac{cos\,\theta}{\sqrt{3}} - \frac{sin\,\theta}{3}\right)q + p - \frac{B}{A} \quad (2)$$

where p represents the mean stress, q the generalized deviatoric stress and θ the Lode's angle, A and B two independent parameters (A = m σ_c and B = s σ_c^2, evaluated at the elastic limit and peak). In this relationship, the geometry of the stresses is considered through the Lode's angle. As a result, the failure criteria can be differentiated according to the compression (θ = π/6) and extension (θ = -π/6) stress paths, as evidenced by laboratory tests carried out on claystone samples (Armand et al. 2017b). In particular, for a mean stress of -12 MPa, the ratio between extension and compression peak strengths is 0.67, which is consistent with the results of laboratory tests.

For residual strength, the same shapes of yield function as the peak are suitable when the confining pressure does not exceed the transition stress between the ductile and softening behaviours, σ_3^{bd}. Beyond this confining pressure, residual strength coincides with the peak criterion. The needed parameters of residual strength (when $\sigma_3 < \sigma_3^{bd}$) are s_r and m_r. By default, s_r is taken equal to 0 and m_r is back-calculated so that the residual strength intercepts the peak shear strength envelope for σ_3^{bd} of confining pressure.

The strain hardening in pre-peak and strain softening in post peak are modelled as a non-linear change (cubic spline) of A with respect to the internal plastic variable γ (from the elastic limit A_i to the peak A_p and from A_p to A_r). We also considered a parabolic evolution of parameter B as a function of γ for the hardening in pre-peak and softening in post-peak, with horizontal tangents at peak and the beginning of the residual phase. Details of the yield function evolution from initial plasticity to peak (pre-peak regime) and then to residual behaviour (post-peak regime) are referred to Souley et al. (2011, 2017). The yield function corresponding to different loading (elastic limit; peak and residual) are shown in Fig. 4b and Fig. 5b.

Under tensile stresses, we propose a «cut-off» of mean stress to the value of tensile strength σ_t (in triaxial condition, which is by default: B/A), this leads to the following yield surface in tension:

$$F_t^{\,m} = p - \sigma_t \quad (3)$$

As a reminder, a quasi-isotropic plastic behaviour can be considered as a first approximation to describe the nonlinear response of the rock matrix. The induced anisotropy due to the change of stresses will be approximated by an assumption of the existence of a weakness plane with a certain orientation. As a result, the independent parameters A and B do not change with the loading direction.

It is known that for most geomaterials, a non-associated flow rule is generally required to reproduce the transition between the contraction and dilation in the plastic volumetric strain. Laboratory tests on COx samples show that the hypothesis of the associated flow rule over-estimates the material dilatancy. Indeed, experimental data exhibit a contractant behaviour (Chiarelli et al. 2003; Zhang and Rothfuchs 2004; Hoxha et al. 2004). At best, a dilatancy develops near the residual strength of the tests carried out under low confining pressures. Contractant or dilatant irreversible deformations are explained by two independent phenomena that occur during the post-pic phase as reported by Conil-Aublivé et al. (2004): the mineral grains deform elastically, and the grains or part of grains move slightly under the applied stress and slide freely relative to each other. From a physical point of view, it is

conceivable that the dilatancy disappears for large deformation, because of a slip along a fracture plane where the roughness has been sheared.

The following plastic potential based on Drucker-Prager form is adopted.

$$G_s{}^m = q + \beta(\gamma)\, p \tag{4}$$

where γ (the internal flow variable) is the plastic distortion, β is the dilatancy rate and varies between an initial value β_0 (elastic limit) and an asymptotic value β_m. The evolution of $\beta(\gamma)$ is given by:

$$\beta(\gamma) = \begin{cases} \beta_m - (\beta_m - \beta_0)e^{-b_\beta \gamma} & \gamma \le \gamma^{ult} \\ \beta_{ult} e^{\left(1 - \gamma / \gamma^{res}\right)} & \gamma > \gamma^{ult} \end{cases} \tag{5}$$

where b_β is the plastic flow velocity, $\beta_{ult} = \beta_m - (\beta_m - \beta_0)e^{-b_\beta \gamma^{ult}}$ and γ^{ult} defined below.

For high levels of deformation, it can be physically expected that the dilation will disappear and a purely frictional behaviour resulting from the complete shearing of the roughness on the fracture surfaces (or the shear band) thus created. In order to account for the sliding along the fracture plane after a significant relative displacement (or plastic strain), a loss of dilation (i.e. shearing at constant volume) is then imposed. The ultimate plastic strain from which the dilatancy decreases is noted γ^{ult}. Beyond this plastic deformation, the dilatancy rate gradually decreases and tends asymptotically to zero.

Finally, an associated flow rule is assumed in tension.

$$G_t{}^m = p \tag{6}$$

Equations (2) to (6) associated with the hardening/softening flow and a transition between brittle and ductile responses, allow to describe the nonlinear behaviour of the matrix.

We designate (m_p, s_p) and (m_r, s_r) as the values of parameters (m, s) at the peak and the beginning residual phase. Assuming a transition between brittle and ductile behaviour for high confining pressure ($\sigma_3 > \sigma_3{}^{b\text{-}d}$ representing the brittle/ductile transition), residual strength must coincide with the peak strength. Consequently, equation (1) for peak and residual strengths makes it possible to express a relationship between the peak and residual strength parameters:

$$m_r = m_p + \left(s_p - s_r\right)\frac{\sigma_c}{\sigma_3{}^{bd}} \tag{7}$$

3.3. Case of weakness planes (induced anisotropy)

In this study, the failure criterion on the weakness plane is a combination of Mohr-Coulomb envelope with strength «cut-off» in tension (i.e. Rankine criterion). Obviously, the tensile strength of these discontinuities should be lower than the value of $C_{wp}/tan(\varphi_{wp})$, which is the intersection between the Mohr-Coulomb yielding and the horizontal axis in plane (σ_{nn}, τ) (with C_{wp} and φ_{wp} are the cohesion and friction angle of the weakness planes). This is

justified since we can associate each plane of weakness as a dilatant (or not) rock discontinuity (depending on its roughness type: primary and/or secondary).In the literature, more complex criteria have been considered (Duveau and Shao 1998; Prassetyo et al. 2017). The projection of a state of stress on the combination envelope is controlled by a non-associated flow rule for shear plastic behaviour and an associated flow one for tensile plastic behaviour.

The local system (s, t, n) of reference axes is defined by the weakness plane consisting of (s, t) and n the outward unit normal of this plane. The magnitude of the tangential (shear) stress component on the weak plane, and the associated shear strain variables are:

$$\tau = \sqrt{{\sigma_{sn}}^2 + {\sigma_{tn}}^2} \quad \text{and} \quad \gamma^{wp} = \sqrt{{\varepsilon_{sn}}^2 + {\varepsilon_{tn}}^2} \tag{8}$$

The generalized stress vector used to describe the weak-plane yield surface has four components: σ_{ss}, σ_{tt}, σ_{nn}, τ. The components of the corresponding generalized strain vector are: ε_{ss}, ε_{tt}, ε_{nn}, γ^{wp}. The weakness plane yield function with a tension cut-off is expressed in terms of (σ_{nn}, τ) as follow:

$$\begin{cases} {F_s}^{wp} = \tau + \sigma_{nn}\, tan\left(\varphi_{wp}\right) - C_{wp} \\ {F_t}^{wp} = \sigma_{nn} - {\sigma_t}^{wp} \end{cases} \tag{9}$$

where ${\sigma_t}^{wp}$ is the tensile strength of the weakness plane.

The potential function is composed of two functions used to define shear (non-associated) and tensile (associated) plastic flow:

$$\begin{cases} {G_s}^{wp} = \tau + \sigma_{nn}\, tan\left(\psi_{wp}\right) \\ {G_t}^{wp} = \sigma_{nn} \end{cases} \tag{10}$$

where ψ_{wp} is the weakness plane dilation angle.

We assume that, the dilatancy rate along the weakness plane is constant and equal to $\tan\left(\psi_{wp}\right)$ during the softening stage of the rock matrix ($\gamma^{wp} \leq \gamma^{ult} - \gamma^{peak}$). Beyond to this deformation threshold, the dilatancy rate of weakness plane starts to decrease:

$$tan(\psi) = \begin{cases} tan\left(\psi_{wp}\right) & \gamma^{wp} \leq (\gamma^{ult} - \gamma^{peak}) \\ tan\left(\psi_{wp}\right) e^{\left(1 - {\gamma^{wp}}/{(\gamma^{ult} - \gamma^{peak})}\right)} & \gamma^{wp} > (\gamma^{ult} - \gamma^{peak}) \end{cases} \tag{11}$$

The orientation of weakness plane depends on the stress state, which is determined according to the assumption presented in section 3.1 (see Fig. 2b).

3.4. Numerical implementation and verification

The proposed model is implemented according to the assumption of small strain. The total strain increment $d\underline{\varepsilon}$ can be subdivided in an elastic part $d\underline{\varepsilon}^e$ and a plastic part $d\underline{\varepsilon}^p$:

$$d\underline{\varepsilon} = d\underline{\varepsilon}^e + d\underline{\varepsilon}^p \quad \text{with} \quad d\underline{\varepsilon}^p = \lambda \frac{\partial G}{\partial \underline{\sigma}} \tag{12}$$

where λ is the plastic multiplier and G is the plastic potential for shear or tensile plastic flow, for both solid rock and weakness plane.

If $\underline{\underline{C}}$ represents the fourth order elastic compliance tensor for transversely isotropic geomaterial, the incremental expression of Hooke's law in terms of generalized stress and strain tensors has the form:

$$d\underline{\sigma} = \underline{\underline{C}}\, d\underline{\varepsilon}^e = \underline{\underline{C}} \left(d\underline{\varepsilon} - d\underline{\varepsilon}^e \right) \tag{12}$$

Finally, the consistency condition $dF(\kappa, \underline{\sigma}) = 0$ allows to express the stress increment as a function of total strain increment:

$$d\underline{\sigma} = \left[\underline{\underline{C}} - \frac{\left(\underline{\underline{C}} : \frac{\partial F}{\partial \underline{\sigma}} \right) \otimes \left(\underline{\underline{C}} : \frac{\partial G}{\partial \underline{\sigma}} \right)}{\frac{\partial F}{\partial \underline{\sigma}} : \underline{\underline{C}} : \frac{\partial G}{\partial \underline{\sigma}} - \frac{\partial F}{\partial \kappa} \frac{\partial G}{\partial \varpi}} \right] d\varepsilon \tag{13}$$

where F is the yield function; κ is the accumulated plastic strain (e.g. γ for the matrix rock or γ^{wp} for the weakness plane); ϖ is the generalized deviatoric stress (i.e. q for the matrix rock and the tangential stress (τ) for the weakness plane).

For both rock matrix and weakness planes yield surfaces, a function representing the bisector between domains $F_s > 0$ and $F_t > 0$ (see Fig. 2b and Appendix A) is evaluated in order to select the type of failure (in shear or in tension). At each step, the computation of new stresses is achieved by testing firstly the yield functions in the solid matrix, then along the plane of weakness. More precisely, the main algorithm is recapitulated below.

- First approximation of stress tensor $\underline{\sigma}^i$, is evaluated by adding to the previous stress tensor the stress increment computed from the total strain increments and the Hooke's law.
- Computation of the yield function for rock matrix, $F^m(p^i, q^i, \theta^i)$ according to equations (2) and (3) respectively for shear and tension failure. If the stress state, $\underline{\sigma}^i$, satisfies the yield criterion: $F^m(p^i, q^i, \theta^i) > 0$, the new increment of stresses is computed as well as the new stress tensor, $\underline{\sigma}^o$. If $F^m(p^i, q^i, \theta^i) \leq 0$, the current stress components are: $\underline{\sigma}^o = \underline{\sigma}^i$.

The resulting stress tensor, $\underline{\sigma}^o$, is then examined for yield function on the weak plane.

- Corresponding stress components in the local axes, $\underline{\sigma}'^o$, are computed using the transformation from global coordinate system (x, y, z) to the local one (s, t, n).
- Computation of the yield function for weak plane, $F^{wp}(\sigma_{nn}'^o, \tau'^o)$ according to equation (9). If the stress state $\underline{\sigma}'^o$ verifies the yield criterion $F^{wp}(\sigma_{nn}'^o, \tau'^o) > 0$, the new increment of stresses is computed as well as the new stress tensor, $\underline{\sigma}^n$. If $F^{wp}(\sigma_{nn}'^o, \tau'^o) \leq 0$, the current new stresses are: $\underline{\sigma}^n = \underline{\sigma}'^o$.
- Back to global coordinate system (x, y, z).

- Parameters depending on the internal plastic variables are updated.

This routine has been written in C^{++} and compiled as a Dynamic Link Library (DLL) file that can be loaded whenever it is needed.

All parameters for the rock matrix have been already identified from triaxial tests for the short-term response (Su 2003; Chiarelli et al. 2003; Armand et al. 2017b; Souley et al. 2017) and summarized in Table 2. Note that results of laboratory tests showed a wide variability of plastic strains, elastic limit, peak and residual strengths. The fitting of the parabolic criterion of Hoek and Brown (1980) based on these experimental data, allows to propose two sets of parameters m, s and σ_c (even-though remember, these parameters no longer have the same meaning as the original Hoek and Brown definition) for the elastic limit and peak strength: one called "average" that was obtained by best fit of Hoek and Brown criterion from the experimental data and the other called "lower" which represents the lower bound of the experimental data. Regarding parameters related to the failure along planes of weakness, they are currently not able to be calibrated based on the laboratory tests. These parameters are chosen in the way that the modelling can reproduce the observations in the convergence and the fractured zone of both drifts GCS and GED. However, the characterization of the weakness plane parameters deserves further attention in future studies. The elastic characteristics along the planes of weakness are considered identical to those of the matrix as by default: $E_s=E_1$ (with E_1, E_s are Young moduli in the bedding plane of the rock matrix and of weakness plane); $E_n=E_3$ (E_3, E_n are Young moduli in the direction normal direction to the bedding plane of the rock matrix and weakness planes; $G_{13}=G_{sn}$ (G_{13}, G_{sn} are shear moduli in the anisotropic plane of the rock matrix and weakness plane); $\nu_{12}=\nu_{st}$ and $\nu_{13}=\nu_{sn}$ (Poisson coefficient respectively in the isotropic and anisotropic planes). Table 2 provides the list of parameters and input values.

In order to verify the proposed model in terms of constitutive equations and numerical implementation, triaxial compression tests with different confining pressures (0.01, 1, 2, 5, 10, 20, and 30 MPa) are simulated. Fig. 3a presents the corresponding deviatoric stress - axial, lateral and volumetric strain curves for different confining pressure, while Fig. 3b shows the results of laboratory tests in terms of deviatoric stress versus axial displacement recorded by external sensors. The simulations were performed with the "best-estimated" values of the parameters s_i, σ_{ci}, m_i, s_p, σ_{cp}, and m_p for the elastic limit and the peak strength. It can be seen that the mean values of the input strength parameters quantitatively reproduce the experimental curves.

The simulations of triaxial compression were also used to verify the proposed model without and with the presence of weakness planes (see Fig. 4 and Fig. 5), where the input parameters are those listed in Table 1. As observed in Fig. 4a, the post-peak behaviour is confining pressure dependent and the transition stress between brittle failure and ductile behaviour is clearly marked for an input value of transition stress σ_3^{bd} about 25 MPa. The resulting curves display four stages (elastic, hardening in pre-peak, softening in post-peak and residual phases) when the confining pressure is below the transition stress level σ_3^{bd}, but only three stages (elastic, hardening and perfect plastic phase) under high confining pressure.

As shown in Fig. 5a, the ubiquitous joints make the material more brittle. The failure of weakness planes occurs only in the post-peak stage of the rock matrix. The behaviour along the planes of weakness is frictional (sliding)

and without dilatancy ($\psi_{wp} = 0$): which explains the contracting character of volumetric strain for simulations at 2 and 5 MPa of confinement (Fig. 5a). A dilatant behaviour like that in Fig. 4a should have been obtained if the dilatancy along planes of weakness is taken equal to that of the intact matrix. Hence, these joints are automatically deactivated when the confining pressure exceeds the transition stress σ_3^{bd}.

Comparisons between the values of the elastic limit, the peak and the residual strengths for different confining stress in Fig. 4a and Fig. 5a, and the theoretical curves described by equations (2) and (8) are given in Fig. 4b and Fig. 5b. A perfect agreement can be observed for numerical and analytical solutions since the relative error for peak strength is less than 0.1%, and 3% for the elastic limit and the residual strength.

4. Application to Meuse/Haute-Marne URL drifts

4.1. Geomechanical model of GCS and GED drifts and numerical issues

This section is devoted to applying the current model for 3D structure modelling of two drifts GCS ($//\sigma_H$) and GED ($//\sigma_h$) in the URL. The localisation of these two drifts with the URL is shown in Fig. 1. The non-triaxial of revolution stress paths must occur when considering the excavation of underground cavities. Drifts' geometry is characterized by a radius of 2.6 m (average value of the radii of the two drifts) and a length of 32 m (even if the GED gallery is 71 m long). The drift centres are located at the depth of 490 m. The far field stress tensor is σ_H = 16.1 MPa; σ_h = 12.4 MPa; σ_v = 12.7 MPa at the depth of URL (Wileveau et al. 2007).

The difference between GCS and GED consists in the drift orientation, the drift geometry (circular with a radius of 2.6 m for GCS and horseshoe geometry with a radius of 2.3 m for GED) and drift support (bolt, hanger and thin shotcrete for GCS versus bolt, 20 cm shotcrete and compressible wedge for GED). The support is not modelled, and a circular geometry of 2.6 m radius is considered for both drifts. Anisotropic responses around these two drifts due to the excavation, have been shown by exhaustive in-situ monitoring. The field observations about EFZ and ~ 10 years of measurement in convergences of these two drifts are shown in Fig. 6, Fig. 7 and Fig. 8 (Armand et al. 2013; 2014). As mentioned in the introduction, these anisotropic responses of the COx claystone have been of interest for several research teams for more than 10 years (Seyedi et al. 2017). All the teams have used a 2D strain plane approach with the convergence-confining method so far. Moreover, the reproduction of the field observation for both drifts GCS and GED with an identical set of material parameters has been still challenging.

A purely mechanical instantaneous simulation is considered, without time effect due to hydro-mechanical couplings and creep behaviour. As a reminder, the pore pressure distribution from an instantaneously coupled hydro-mechanical simulation can be deduced exactly from a purely mechanical simulation for a poroelastic behaviour of material; and approximately for a poroelastoplastic behaviour of material (Vu et al. 2020a, b).

The excavation is simply carried out in 32 steps where 1 m of material is cut along the tunnel for each step. The model geometry and mesh are displayed in Fig. 9. The geometrical model (68 m high, 34 m wide and 58 m long) involves 270,000 elements with the following characteristics: the element size consists of (a) 9 cm radially and tangentially around the walls of drifts; (b) in the first crown (COx_a in Fig. 9a) between radius 2.6 and 9 m, the element size increases radially from 9 to 30 cm, and from 30 cm to 1,8 m inside the domain COx_b, and so on;

and (c) 50 cm axially in the central part of the geometrical model. This element size was chosen based on our experience feedback, which recommends a representative global response of the observations with a reasonable computation time. It is known that simulations of the post-peak behaviour of geomaterials with continuous approaches lead to results that are strongly dependent on the mesh used. This has led, during the last two decades, to the development of methods and numerical tools to overcome this problem. We can cite three different solutions to overcome this problem from the numerical point of view: (a) calibration on the fixed grid structure (mesh resolution should be constant for any model using one calibrated data set). In other words, "calibrate" the model against the behaviour of a known case or own feedbacks; (b) adaptative re-meshing inside the localisation (mesh refinement), (c) extension of the constitutive model by internal scaling parameter (regularization), mainly: Cosserat theories, gradient theories and nonlocal approaches. These methods are widely developed and applied with success in several "house" and industrial finite element codes (Manica et al. 2018; Manica et al. 2021a, b ; Pardoen and Collin 2017; Yu et al. 2021a, b), but not in finite difference codes except the works of Alehossein and Korinets (2000) and Postill et al. (2021) on the local and non-local gradient approaches respectively, using the Mohr-Coulomb constitutive model with strain softening in *FLAC*. In this paper it is the first numerical solution (calibration on the fixed grid structure) that is used. More precisely, in the area of interest around the excavation, the residual plastic deformation is assumed to be a function of the volume elements divided by a reference volume V_0 usually taken equal to 0.1(unit of length) x 0.1(unit of length) x 0.5(unit of length) based on our feedback.

The initial in situ stresses are introduced in the model according to the depth. A zero normal displacement condition is applied for the bottom and lateral surfaces. The vertical stress corresponding to the overburden weight is applied on the top surface of the model.

The proposed phenomenological anisotropic model remains continuous, therefore not well suitable to describe the networks of explicit fractures induced underground excavations. The biaxial, triaxial and radial extension tests performed by Zhang (2016), Desbois et al. (2017), Zhang et al. (2019) clearly showed the formation of clear fracture planes (individual or conjugate) in the post-peak phase and at the end of tests (Zhang et al. 2019). Indeed, the measurement of the permeability during a triaxial compression test exhibits that the permeability changes slightly during the elastic and the plastic hardening stages (Zhang 2016, Zhang et al. 2019); but increases drastically with the post-peak (plastic softening and residual) stages due to the occurrence of the induced cracks and shear bands. Besides, de la Vaissière et al (2015) showed a considerable increase in permeability in the ZFC and a moderate increase in permeability in the ZFD compared to the intact rock. Therefore, the zone close the gallery wall, where the excavation induces softening and residual regimes, can be considered as the ZFC, while the zone where only hardening regime is reached after the excavation, is assumed to be ZFD, with the type of the proposed model.

Unlike the 2D configuration approach, 3D simulation yields the 3D characteristics of results, i.e. EFZ and convergence change from one cross section to another.

To localise a section, we introduce two parameters: *l* is the distance of the considered section to the beginning of the drift; *h* is the distance between the face advance (or tunnel front) to the considered section. *h* varies from a negative value to a positive one when the face advance is before and after the considered section, respectively.

Five cross sections (1 to 5) of GCS and GED drifts will be examined in detail in terms of the plastic zones extension, the horizontal and vertical convergences and their ratio. They are located at l = 5.5, 10.5, 15.5, 20.5 and 26.5 m. From the numerical point of view, different zones can be distinguished around the drifts. Pre-peak zone (termed by Hard state) corresponds to the domain of elements for which the mechanical behaviour remains in the pre-peak region after the initiation of plasticity. Failed zone (termed by Soft state) contains the elements with a post-peak behaviour (with failure along the weakness planes in shear or tension depending on the local stress state acting on the potential weakness plane). Fractured zone (termed by Residual state) when the residual regime is reached and finally tensile zone (termed by Tensile) for failure in tension. As previously stated, and for the sake of comparison with the in situ observations, these different zones are grouped together as follows: the numerical failed and fractured zones in ZFC domain, and pre-peak zone in terms of ZFD domain. Several different convergence criteria are available in *FLAC*^{3D} to determine when equilibrium is reached (Maximum Out-of-Balance Force, Local Force Ratio, Average Force Ratio and Maximum Force Ratio). Each of these is based on the out-of-balance force acting on the grid points (structural nodes). At equilibrium which reflects the numerical convergence of each excavation phase, the maximum out-of-balance force is almost zero. If the unbalanced forces approach a constant nonzero value, this indicates that failure and plastic flow are occurring within the model. In the numerical simulations, two of these criteria were systematically used at each of the 32 excavation stages of the GCS and GED drifts: (a) when the decrease of the Maximum Out-of-Balance Force reaches a plateau, and (b) when the Maximum Force Ratio, defined as the maximum out-of-balance force divided by the average total force acting on all grid points, is less than 10^{-5}.

In addition, for each drift, a total of 32 sequential excavation steps of one meter in length are performed. Each excavation sequence requires approximately 1 hour to reach equilibrium on a 3.20 GHz Intel (R) Xeon (R) computer. The total computation time is approximately 32 hours.

4.2. Results of GCS and discussion

The GCS drift, excavated in the direction of the principal horizontal major stress (σ_H), is prescribed by quasi-isotropic far field stress with a ratio of initial stresses σ_h/σ_v of 0.98. An isotropic rheological model generally leads to quasi-isotropic extension of EFZ and convergence, as reported in the benchmarking of the constitutive models developed for the COx claystone behaviour and summarized in Seyedi et al. (2017). This is the case when an isotropic version of the proposed model is used (Souley et al. 2017) which differs from the in situ observations as shown in Fig. 6 and Fig. 8. The proposed model takes into account the anisotropy in stiffness, but the plastic behaviour of the rock matrix is isotropic. However, the introduction of weakness planes allows reproducing of the induced anisotropy as shown below.

Fig. 10 to Fig. 13 show the predicted plastic zones around the GCS drift. The first two figures represent the extensions of plastic zones at the end of the excavation. Whereas, the two last figures show the plastic zones for two cross sections (GCS1 and GCS3) at l = 5.5 and 15.5 m for different values of h.

Fig. 10 represents the numerically predicted distributions of ZFC and ZFD according to the previous analogy assumed between the plastic zones in pre and post peak regimes and the in situ observations of connected and diffuse fracture zones. The three-dimensional character of these zones is clearly highlighted. In particular, the cross sections GCS1 and GCS3 which are the most representative of the first 4 of 5 cross sections (Fig. 12) for different face advance are examined for h = +5.5 m (~1xD), +10.5 m (~2xD) and at the end of the excavation. When the face reaches the section positions (i.e. h=0) (Fig. 12a, Fig. 13a), the plasticity limited to the pre-peak behaviour develops at the forehead, as well as radially in the first 2 to 3 elements from the drift wall with extensions of 20 and 30 cm (or 0.02xD and 0.04xD), for the roof-floor and the right side. For h = 1xD, the extension of ZFC consists of one element (at section GCS3 l = 15.5 m) and 2 elements (at section GCS1 l = 5.5 m) corresponding to 9 and 20 cm at the roof-floor. Beyond the distance h = 1xD, the extent of ZFC remains constant. Conversely, on the right side, this zone extends from 60 to 90 cm (i.e. 0.1xD to 0.17xD) when then the tunnel front advances from h = 1xD to the end of the excavation. Therefore, there is anisotropy of ZFC extension between the roof-floor and the sides as observed around the M/HM URL structures (Armand et al. 2013, 2014).

The examination of the ZFD in Fig. 12 and Fig. 13 shows its evolution as a function of the face advance and its anisotropy between the roof-floor and sides. In particular, at h = 1 m from the sections, ZFD extensions are 1.4 m and 1.7 m (or 0.26xD and 0.32xD) at the roof-floor and sides. The ZFD extent no longer increases beyond one diameter at the roof-floor (with an extension of 1.5 m): which is not the case for the sides.

The extensions of ZFD and ZFC around the first 4 sections of the GCS drift were analysed in detail at the end of the excavation. Table 3 summarizes these extensions obtained from the numerically predicted extent of plastic zones for both intact matrix and weakness planes developing during the post-peak phase. We notice that the extension of the pre-peak plastic domain (or ZFD) is about 0.3xD, 0.4xD and 0.3xD respectively at the roof, sides and floor. These values remain close to the lower limit of the range of variation of the ZFD extensions observed in situ by Armand et al. (2014) and recalled in Table 1. The extension of the post-peak plastic domain (or ZFC) including shear and tensile failure along the weakness planes, is about 0.04xD, 0.2xD and 0.04xD respectively at the roof, sides and floor. These values also remain in the range of variation of the ZFC extensions observed in situ (Table 1). Specifically, they correspond to the average values measured in the floor-roof and sides of GCS drift. Finally, the anisotropy is more pronounced for post-peak behaviour. Macrocracks essentially develop close to the sidewall of drift, which, in turn, affects the magnitude of convergences.

Fig. 14a shows the numerical result of the evolution of vertical and horizontal convergences around the GCS drift for sections 1 to 5 (with l = 5.5, 10.5, 15.5, 20.5 and 26.5 m). These are cumulated convergences according to the face advance from h = 0.5 m to the end of the excavation. The modelling result of the ratio between horizontal and vertical convergences is reported in Fig. 14b.

As illustrated above (Fig. 12 and Fig. 13), the ZFC extent at the GCS sides continues to increase beyond h = 2xD in relation to the induced damage (failure along weakness planes) which develops according to the magnitude of the induced stresses. Cross sections 4 and 5 (l = 20.5 and 26.5 m) remain influenced by the end of the excavation. Conversely, the first two sections (1 and 2) located at a distance less than 2xD from the beginning of GCS, seem to be also affected by this proximity. Consequently, section 3 located in the middle of the gallery can be considered

as the most representative. The final instantaneous horizontal convergence predicted by the proposed model is about 29 mm, which is very close to the value of ~ 26 mm (2 x 13 mm) measured during the Mine-by experiment set up around GCS drift (Armand et al. 2013) (see Fig. 15) and higher than about14 mm obtained by Guayacan-Carrillo et al. (2016a), where they interpreted the in situ measurements by the semi-empirical model proposed by Sulem et al. (1987). As a reminder, Guayacan-Carrillo et al. (2016a) proposed the instantaneous horizontal and vertical convergences: C_h (horizontal convergence) from 9.3 mm to 14.0 mm and C_v (vertical convergence) from 4.8 mm to 7.5 mm when they calibrated the empirical convergence model for GCS drift.

The slight difference between our prediction and the measurements can be explained by the fact that the numerical model did not take into account the flexible support and the bolt set up during the excavation of GCS. The predicted vertical convergence is about 16.5 mm, which leads to a convergence anisotropy ratio of 1.72. This value remains in the range of convergence ratios observed in situ.

4.3. Results of GED and discussion

Fig. 16-Fig. 19 illustrate the predicted extent of plastic zones around the GED drift. The anisotropic shape of the plastic zone is more pronounced than the quasi isotropic shape of GCS drift. This is due to the difference between the anisotropy ratios of the initial stresses within the section of the drift (1.3 for GED versus 1.02 for GCS).

More precisely, Fig. 16 summarizes the numerically predicted distributions of ZFC and ZFD around GED. Similar to the case of GCS drift, the three-dimensional nature of their formations is again clearly highlighted, which is described by the change of the EFZ from one section to another. The EFZ of cross sections GED1 (l = 5.5 m) and GED3 (l = 15.5 m) corresponding to different face advance positions: h = +5.5 m (~1 D), +10.5 m (~2 D) and at the end of the excavation, are examined in details.

Once the face reaches the section position (Fig. 18a, Fig. 19a), only pre-peak plastic (Hard state) zones develop around the entire drift circumference, with the extents of 0.05xD, 0.17xD and 0.17xD at the side wall, roof and floor of GED. Then, zones with post-peak behaviour (ZFC) initiate and develop around GED and the extents of the ZFC and ZFD become increasingly anisotropic when the excavation progresses. When the face reaches a distance h = 2xD from the section (1 or 3), the ZFC extends to 0.02xD, 0.3xD and 0.2xD at the side wall, roof and floor of GED. Beyond this distance h = 2xD, the ZFC extent no longer increases.

Table 4 summarizes the extent of ZFC and ZFD from the predicted extent of plastic zones. One can notice that the extension of the plastic domain (including both ZFC and ZFD zones) is about 0.6xD, 0.3xD and 0.6xD respectively at the roof, sides and floor. As for the GCS drift, these values remain in the range of variation of the ZFD extensions observed in situ and specified in Table 1 (Armand et al. 2014). Indeed, they correspond to the average values measured around the GED drift.

The extension of the post-peak plastic domain (or ZFC) is about 0.3xD, 0.02xD and 0.3xD respectively at the roof, sides and floor, which are also found in the range of variation of the ZFC extensions observed in situ (Table 1). Once again, they correspond to the average values measured in the floor-roof of GED drift. Even if the predicted

extension of ZFD appears to be underestimated with respect to the in situ observations, it can be evoked that the proposed model reproduces relatively well the extensions of the fractured zones observed around the GED drift.

Fig. 20a displays the evolution of vertical and horizontal convergences of GED drift for sections 1 to 5, according to the face advance. In the direction of the initial principal minor stress in the cross section (i.e. horizontal for GCS and vertical for GED), the difference in the convergence between these five considered sections is less important in the case of GED compared to the GCS drift. This is explained by the anisotropy of the initial stresses. The absolute values of the instantaneous convergences obtained by the proposed model are found in the range: 45 mm to 50 mm for C_v and 17 mm to 24 mm for C_h. Guayacan-Carrillo et al. (2016a) taken the instantaneous convergences in the range: 24.5 mm to 32.2 mm for C_v and 5.3 mm to 8.4 mm for C_h. The numerical predicted ratio between vertical and horizontal convergences is shown in Fig. 20b, which is in the region of 2.3.

As a conclusion, the proposed model reproduces fairly well, with a sole set of parameters, the absolute instantaneous convergences (C_h, C_v) and the ratio C_h/C_v for both drifts GCS and GED; the EFZ (ZFC and ZFD) for GED drift. The anisotropic shape of EFZ should be improved. The incorporation of the damage mechanics (coupling between the plasticity in pre-peak behaviour and the damage in the post-peak behaviour); as well as the non-local modelling have been considered to improve the modelling of the EFZ around GCS. Moreover, the 3D simulation allows avoiding the concept of convergence-deconfining curve used in the 2D simulation. This curve represents the deconfining ratio versus the distance from the advancing tunnel front to the considered section. The calibration of this convergence-deconfining curve is not a trivial task. Many theoretical and numerical works have been performed to propose an empirical equation for this curve for a tunnel within an elastoplastic rock. However, these empirical equations were usually obtained with the assumption of a circular plastic zone. This is not the case for GCS and GED drifts within the URL. Moreover, the 3D simulation gives 3D results about the excavation induced fractured zones and the convergence which change from one section to another, as well as the stress-strain state and plastic zone behind the tunnel front, which cannot be evaluated with 2D simulation.

5. Conclusion and perspectives

This paper presents the development of an anisotropic constitutive model for transversely isotropic geomaterials, its numerical implementation in the three-dimensional code *FLAC^{3D}*, its verification and calibration, as well as its application in the 3D simulation of two drifts in the URL: GCS ($//\sigma_H$) and GED ($//\sigma_h$). Firstly, a non-linear elastoplastic model, based on the observation from the laboratory test performed on the COx sample, using the Hoek and Brown failure criterion, is presented. The elastic anisotropy, the almost isotropy of strength observed on the available tests carried out in several directions, the induced anisotropy observed on the in situ structures are the main ingredients for this model. The rock matrix behaviour is characterized by a non-linear behaviour in pre peak, a non-linear softening in post-peak and perfectly plastic behaviour in the residual phase. The model also takes into account the transition between the strain softening in post-peak under low and moderate confining pressures and the ductile behaviour under high confinements.

Simulation of triaxial compression tests at different levels of confining pressure provides a verification of the implemented model. The resulting curves display four regions (elastic, hardening in pre-peak, softening in post-

peak and residual phase) when the confining pressure is below the transition stress, and three regions (elastic, damage and perfect plastic phase) under high confining pressure. The introduction of induced anisotropy through the concept of weakness planes in post-peak phase was highlighted in the simulations on triaxial compression tests. In addition, the elastic limit, the peak and residual strengths derived from these simulations are compared with the theoretical curves in plan *p-q* (mean-deviatoric stresses): the corresponding relative error does not exceed 1%.

Model parameters calibrated from the triaxial test on sample scale were used to model the mechanical responses of COx claystone due to the excavation. For this purpose, two drifts GCS and GED within URL were considered, where exhaustive monitoring information about the convergence and fractured zones are available. The modelling is three-dimensional, which is advantageous with respect to previous plane strain models. Indeed, the present 3D model allows gaining more insights regarding the fractured zone development after the front advancement during the excavation, the variation of convergence and the induced fracture zone along the tunnel axis. The proposed model reproduces fairly well the short term convergence, as well as the anisotropy in the ratio of convergence for these two galleries with respect to the measurement. Moreover, the ability of the implemented model to describe the plastic zones around an underground drift excavated in the Callovo-Oxfordian claystone is rather successfully tested, particularly for GED drift (// horizontal minor stress). The reproduction of the fractured zone around GCS drift exhibits a limitation of the present model, which should be improved in particular by examining more closely the weakness plane parameters for which we lack feedbacks. The results provide new insights on the understanding of the deformation mechanisms observed around the structures of Meuse/Haute-Marne Underground Research Laboratory.

The next step will be to enrich the proposed model on the basis of new knowledge and experimental data, and/or other phenomena that have not been taken into account here (damage in the framework of damage mechanics, time-dependent behaviour, hydromechanical couplings, etc.).

6. References

Abdi H, Labrie D, Nguyen TS, Barnichon JD, Su G, Evgin E, Simon R, Fall M (2014) A laboratory investigation on the mechanical behaviour of the Tournemire argillite. Can Geotech J, 10.1139/cgj-2013-012

Alehossein and Korinets (2000) Gradient dependent plasticity and the finite difference method. Commun. Numer. Meth. Engng 2000; 16:363-375

Armand G, Bumbieler F, Conil N, Cararreto S, de la Vaissière R, Noiret A, Seyedi D, Talandier J, Vu MN, Zghondi J (2017a) The Meuse\Haute-Marne underground research laboratory: Mechanical behavior of the Callovo-Oxfordian claystone. Rock Mechanics and Engineering Volume 2: Laboratory and Field Testing, edited ByXia-Ting Feng

Armand G, Dewonck S, J-M, Bosgiraud, Richard-Panot L (2015) Development and new research program in the Meuse Haute Marne Underground Research Laboratory (France). 13th ISRM International Congress of Rock Mechanics

Armand G, Leveau F, Nussbaum C, de La Vaissiere R, Noiret A, Jaeggi D, Landrein P, Righini C (2014) Geometry and properties of the excavation induced fractures at the Meuse/Haute-Marne URL drifts. Rock Mech Rock Eng 47(1):21–41. doi:10.1007/s00603-012-0339-6

Armand G, N Conil, Talandier J, Seyedi DM (2017b) Fundamental aspects of the hydromechanical behaviour of Callovo-Oxfordian claystone: from experimental studies to model calibration and validation. Computers and Geotechnics 85:277-286

Armand G, Noiret A, Zghondi J, Seyedi DM (2013) Short- and long term behaviors of drifts in the Callovo-Oxfordian claystone at the Meuse/Haute-Marne Underground Research Laboratory. J Rock Mech Geotech Eng 5(3):221–230

Armand, G, Bumbieler F, Conil N, de La Vaissière, Bosgiraud JM, Vu, MN, (2017c), Main outcomes from in situ THM experiments programme to demonstrate feasibility of radioactive HL-ILW disposal in the Callovo-Oxfordian claystone, J Rock Mech Geotech Eng, 9(3), 415-427

Bandis SC, Barton NR, Christianson M (1985) Application of a New Numerical Model of Joint Behaviour to Rock Mechanics Problems. in Fundamentals of Rock Joints Björkliden, Sweden, September 1985, pp. 345-356

Bésuelle P, Lanata P (2014) Characterization of the early strain localization in a sandstone and a clay rock. Cambridge, UK, 1-3 September 2014

Boehler, J.P., and Sawczuk, A. (1977) On Yielding of Oriented Solids, Acta Mechanica, 27, 185-206

Chang L, Konietzky H (2018) Application of the Mohr-Coulomb Yield Criterion for Rocks with Multiple Joint Sets Using Fast Lagrangian Analysis of Continua 2D (FLAC2D) Software. Energies 2018, 11, 614

Chiarelli AS, Shao JF, Hoteit N (2003) Modelling of elastic-plastic damage behaviour of a claystone. Int J Plast 19:23–45

Conil-Aublivé N, Djeran-Maigre I, Cabrillac R, Su K (2004) Poroplastic damage model for claystones, Applied Clay Science, 26:473-487

David C, Robion P, Menendez B (2005) Anisotropy of elastic, magnetic and microstructural properties of the Callovo-Oxfordian shales (Meuse). in: 2nd Int Meeting Clays in Natural & Engineered Barriers for Radioactive Waste Confinement

de la Vaissière R, Armand G, Talandier J (2015) Gas and water flow in an excavation-induced fracture network around an underground drift : A case study for a radioactive waste repository in clay rock. Journal of Hydrology 521:141-156.

Desbois G., Höhne N., Urai J.L., Bésuelle B. and Viggiani G. (2017) - Deformation in cemented mudrock (Callovo–Oxfordian Clay) by microcracking, granular flow and phyllosilicate plasticity: insights from triaxial deformation, broad ion beam polishing and scanning electron microscopy. Solid Earth, 8, 291–305, 2017

Diederichs MS (2003) Manuel Rocha Medal Recipient Rock Fracture and Collapse Under Low Confinement Conditions. Rock Mech Rock Eng 36:339–381

Diederichs MS (2007) The 2003 Canadian Geotechnical Colloquim : Mechanism interpretation and practical application of damage and spalling prediction criteria for deep tunnelling. Can Geotech J, 44 :1082-1116

Duveau G, Shao JF (1998) A modified single plane of weakness theory for the failure of highly stratified rocks. Int J Rock Mech Min Sci 1998;35(6):807–13

Duveau G, Shao J-F. Henry JP (1998) Assessment of some failure criteria for strongly anisotropic materials. Mech Cohes Frict Mater;3:1–26

Guayacan L-M, Seyedi D, Sulem J, Armand G (2016b) Tunnel excavation in low permeability ground: effect of anisotropy on excess pore pressure, EUROCK 2016

Guayacán-Carrillo L-M, Sulem J, Seyedi, D-M, Ghabezloo S, Noriet A, Armand G, (2016a) Analysis of long-term anisotropic convergence in drifts excavated in callovooxfordian claystone. Rock Mech. Rock. Eng. 49, 97–114

Hill R (1950) The mathematical theory of plasticity. Clarendon Press, Oxford

Hoek E (1983) Strength of jointed rock masses. Geotechnique, 33 (3), 187

Hoek E, Brown ET (1980) Empirical strength criterion for rock masses. J Geotech Eng Div ASCE 106:1013–1035

Hoxha D, Giraud A, Blaisonneau A, Homand F, Chavant C (2004) Poroplastic modelling of the excavation and ventilation of a deep cavity. Int J Numer Anal Meth Geomech. 28:339–364

Ismael M, Konietzky H (2017) Integration of Elastic Stiffness Anisotropy into Ubiquitous Joint Model. Procedia Eng **2017**, 191, 1032–1039

Ismael M, Konietzky H (2019) Constitutive model for inherent anisotropic rocks: Ubiquitous joint model based on the Hoek-Brown failure criterion. Computers and Geotechnics 105 (2019) 99–109

Jaeger JC (1960) Shear failure of anisotropic rocks. Geol Mag, 97, 65

Jaeger JC, Cook NGW (1979) Fundamentals of rock mechanics, 3 ed. Chapman and Hall, London, 593p

Jaeger JC, Cook NGW. Zimmerman RW (2007) Fundamentals of rock mechanics. Fourth edition. Blackwell Publishing, Oxford, 475 p

Lade PV. (2007) Modeling failure in cross-anisotropic frictional materials. *Int J Solid Struct*. 2007;44(16):5146–5162

Lee Y, Pietruszczak S. Application of critical plane approach to the prediction of strength anisotropy in transversely isotropic rock masses. Int J Rock Mech Min Sci 2008;45(4):513–23

Levasseur S, Welemane H, Kondo D (2015) A microcracks-induced damage model for initially anisotropic rocks accounting for microcracks closure. Int J Rock Mech Min Sci 77(2015):122–132

Mánica M., Gens A., Vaunat J. and Ruiz D.-F. (2017) A time-dependent anisotropic model for argillaceous rocks. Application to an underground excavation in Callovo-Oxfordian claystone, Computers and Geotechnics, 85, 341-350

Mánica M., Gens A., Vaunat J. and Ruiz D.-F. (2018) Nonlocal plasticity modelling of strain localisation in stiff clays, Computers and Geotechnics, 103, 138-150

Mánica M., Gens A., Vaunat J., Armand G. and Vu M-N. (2021a) Numerical simulation of underground excavations in an indurated clay using nonlocal regularisation. Part 1: formulation and base case. Geotechnique (accepted).

Mánica M., Gens A., Vaunat J., Armand G. and Vu M-N. (2021b) Numerical simulation of underground excavations in an indurated clay using nonlocal regularisation. Part 2: sensitivity analysis. Geotechnique (accepted).

McLamore R, Gray KE (1967) The mechanical behavior of anisotropic sedimentary rocks. J Eng Indust Trans A.S.M.E., **89**:62

Mróz Z, Maciejewski J (2003) Failure Criteria and Compliance Variation of Anisotropically Damaged Materials. In: Skrzypek, J.J., Ganczarski, A. (eds.) Lecture Notes in Applied and Computational Mechanics, vol. 9, pp. 75–112. Springer, Heidelberg

Mróz, Z., Maciejewski J (2002) Failure criteria of anisotropically damaged materials based on the critical plane concept. Int J Numer Anal Meth Geomech 26:407–431

Nasseri, M.H.B., Rao, K.S. and Ramamurthy, T., 2003. Anisotropic strength and deformational behavior of Himalayan schists. *Int. J. Rock Mech. Min. Sci.*, Vol. 40(1) p. 3-23

Niandou H, Shao J-F, Henry J-P, Fourmaintraux D (1997) Laboratory investigation of the mechanical behavior of tournemire shale. Int J Rock Mech Min Sci 34(1):3–16

Nguyen, T.S., and Le, A.D. (2015) Development of a constitutive model for a bedded argillaceous rock from triaxial and true triaxial tests, *Canadian Geotechnical Journal*, 52, 1072-1086, https://doi.org/10.1139/cgj-2013-0323

Nova R (1980) The failure of transversally anisotropic rocks in triaxial compression. Int J Rock Mech Min Sci Geomech Abstr 17:325–332

Pardoen B, Collin F (2017) Modelling the influence of strain localisation and viscosity on the behaviour of underground drifts drilled in claystone. Computers and Geotechnics 85 (2017) 351–367

Pardoen B., Seyedi D.M. and Collin F. (2015) Shear banding modelling in cross-anisotropic rocks, International Journal of Solids and Structures, 72, 63-87

Pariseau WG (1979) Plasticity theory for anisotropic rock and soils. In: Proceedings of 10th Symposium on Rock Mechanics AIME

Paterson MS (1978) Experimental rock deformation – The brittle field. New York, Springer Verlag, 254p

Pietruszczak S, Lydzda D, Shao J-F (2002) Modeling of inherent anisotropy in sedimentary rocks. Int J of Solids and Struct, 39:637-648

Pietruszczak S, Mróz Z (2000) Formulation of anisotropic failure criteria incorporating a microstructure tensor. Comp. & Geotechnics 24, 105–112

Pietruszczak S, Mróz Z (2001) Formulation of failure criteria for anisotropic frictional materials. Int J Num Anal Meth Geomech 25, 509–524

Postill, H., P.R. Helm, N. Dixon, S. Glendinning, J.A. Smethurst, M. Rouainia, K. M. Briggs, A. El-Hamalawi and A.P. Blake (2021). Forecasting the long-term deterioration of a cut slope in high-plasticity clay using a numerical model. Engineering Geology 280 (2021) 105912

Pouragha M, Wan R, Eghbalian M (2018) Critical plane analysis for interpreting experimental results on anisotropic rocks. Acta Geotechnica https://doi.org/10.1007/s11440-018-0683-0

Prassetyo SH, Gutierrez M, Barton N (2017) Nonlinear shear behavior of rock joints using a linearized implementation of the Barton-Bandis model. J Rock Mech Geotech Eng 9(2017) :671-682

Sainsbury B, Pierce M, Mas Ivars D, (2008) Simulation of rock mass strength anisotropy and scale effects using a Ubiquitous Joint Rock Mass (UJRM) model. Proc 1rst Int. FLAC/DEM Symp Num Modelling, 25–27 August, Minneapolis, USA

Saroglou H, Tsiambaos G (2008) A modified Hoek–Brown failure criterion for anisotropic intact rock. Int J Rock Mech Min Sci 45: 223–234

Sarout J, G,uéguen Y (2008) Anisotropy of elastic wave velocities in deformed shales. Part I: Experimental results. Geophysics 73/5, D75-D89

Seyedi DM, G Armand, Noiret.A (2017) "Transverse Action"–A model benchmark exercise for numerical analysis of the Callovo-Oxfordian claystone hydromechanical response to excavation operations. Computers and Geotechnics 85, 287-305

Shengli L, Wenguang Z, Shanxiong C, Fei Y (2012) Anisotropic Properties Study on Chlorite Schist Using Uniaxial Compression Tests. Int J Earth Sci Eng, 05(05), 1166-1171

Souley M, Armand G, Kazmierczak J-B (2017) Hydro-elasto-viscoplastic modeling of a drift at the Meuse/Haute-Marne underground research laboratoratory (URL). Computers and Geotechnics 85 (2017) 306–320

Souley M, Armand G, Su K, Ghoreychi M (2011) Modeling the viscoplastic and damage behavior in deep argillaceous rocks. J Phys Chem Earth 36(17–18):1949–1959

Su K (2003) Constitutive Models for the Meuse/Haute-Marne Argillites – MODEX- REP, European Commission – Nuclear science and technology, Contract n° FIKW-CT2000-00029, 2-3

Sulem J, Panet M, Guenot A (1987) Closure analysis in deep tunnels. Int J Rock Mech Min Sci Geomech Abstr 24(3):145–154

Tien YM, Kuo MC, Juang CH (2006) An experimental investigation of the failure mechanism of simulated transversely isotropic rocks. Int J Rock Mech Min Sci 2006;43(8):1163–81

Tran Manh H, Sulem J, Subrin D, Billaux D (2015) Anisotropic Time-Dependent Modeling of Tunnel Excavation in Squeezing Ground. Rock Mech Rock Eng (2015) 48:2301–2317

Trivellato E, Pouya A, Vu MN, Seyedi D (2019) A softening damage-based model for the failure zone around deep tunnels in quasi-brittle claystone. In Proceedings "Tunnels and Underground Cities: Engineering and Innovation meet Archaeology", WTC 2019 ITA-AITES World Tunnel Congress, Naples, Italy.

Tsang CF, Bernier F, Davies C (2005) Geohydromechanical processes in the excavation damaged zone in crystalline rock, rock salt, and indurated and plastic clays—in the context of radioactive waste disposal. Int J Rock Mech Min Sci 42(1):109–125

Vu M-N, Armand G, Plua C (2020a) Thermal Pressurization Coefficient of Anisotropic Elastic Porous Media. Rock Mech Rock Eng (2020) 53:2027–2031

Vu M-N, Guayacán-Carrillo L-M, Armand (2020b) Excavation induced over pore pressure around drifts in the Callovo-Oxfordian claystone. European Journal of Environmental and Civil Engineering. doi.org/10.1080/19648189.2020.1784800

Walsh JB, Brace JF (1964) A fracture criterion for brittle anisotropic rock. J. of Geophysical Research, 69 (16), 3449

Wang J, Yu H-S (2014) Three-dimensional shakedown solutions for anisotropic cohesive frictional materials under moving surface loads. Int J Numer Anal Meth Geomech, 38:331–348

Wang T-T, Huang T-H (2009) A constitutive model for the deformation of a rock mass containing sets of ubiquitous joints. Int J Rock Mech Min Sci 46:521–530

Wang T-T, Huang T-H (2014) Anisotropic deformation of a circular tunnel excavated in a rock mass containing sets of ubiquitous joints: Theory analysis and numerical modeling. Rock Mech Rock Eng 47 :643–657

Wileveau Y, Cornet FH, Desroches J, Blumling P (2007) Complete in situ stress determination in an argillite sedimentary formation. Phys Chem Earth 32:866–878

Yao C, Shao JF, Jiang QH, Zhou CB (2017) Numerical study of excavation induced fractures using an extended rigid block spring method. Computers and Geotechnics 85:368-383.

Yu Z, Shao JF, Vu MN, Armand G (2021a) Numerical study of thermo-hydro-mechanical responses of in situ heating test with phase-field model. International Journal of Rock Mechanics and Mining Sciences 138, 104542

Yu Z, Shao JF, Duveau G, Vu MN, Armand G (2021b) Numerical modeling of deformation and damage around underground excavation by phase-field method with hydromechanical coupling. Computers and Geotechnics 138, 104369

Zhang C, Rothfuchs T (2004) Experimental study of the hydro-mechanical behavior of the Callovo-Oxfordian argillite. Applied Clay Science, 26:325-336

Zhang C-L, Armand G, Conil N, Laurich B (2019) Investigation on anisotropy of mechanical properties of Callovo-Oxfordian claystone. Engineering Geology 251 (2019) 128–145

Zhang C-L. (2016) The stress-strain-permeability behaviour of clay rock during damage and recompaction. J Rock Mech. and Geotech. Engng 8(2016) 16-26

Zhang F, Xie SY, Hu DW, Shao JF, Gatmiri B (2012) Effect of water content and structural anisotropy on mechanical property of claystone. Appl Clay Sci 69:79–86

Zhu, Q., and Shao, J.F. (2017) Micromechanics of rock damage: Advances in the quasi-brittle field, *Journal of Rock Mechanics and Geotechnical Engineering*, 9, 29-40

Appendix A. Details on the conceptual model of weakness planes and numerical implementation

Definition of terms plotted in Fig. 2b are recalled below:

σ_t is the prescribed tensile strength, if different to the Hoek and Brown tensile strength, $\sigma_t{}^{HB} = \frac{s\,\sigma_c}{m}$

O: intersection between tensile and shear yield functions

T: tangent to the Hoek and Brown envelope $\mathcal{C}_{HB}$ at point O

L_1 bisects the area bounded by BOT

L_2: vertical line passing through the confining stress of 1 atm

$\boldsymbol{\mathcal{D}_1}$: domain bordered by σ_3-axis, BO segment and the half-line OL_1. $\boldsymbol{\mathcal{D}_1}$ is associated to the tensile failure, with a fracture plane normal to the tensile direction

$\boldsymbol{\mathcal{D}_2}$: domain delimited by OL_1, OA and AL_2. $\boldsymbol{\mathcal{D}_2}$ is associated to the shear failure, with fracture plane oriented normal to σ_3 (i.e. parallel to σ_1-direction, the maximum compressive stress)

$\boldsymbol{\mathcal{D}_3}$: domain delimited by AL_2 and $A\mathcal{C}_{HB}$. $\boldsymbol{\mathcal{D}_3}$ is associated to the shear failure, with conjugate fractures with an angle α_f of $\pm\left(\frac{\pi}{4} - \frac{\varphi_{wp}}{2}\right)$ with respect to σ_1-direction, the maximum compressive stress and φ_{wp} is the internal friction angle of the weak planes.

Finally, line L_1 represents the diagonal between the surfaces $F_s^m = 0$ and $F_s^m = 0$ in the (σ_1-σ_3, σ_3)-plane and divides the complementary domain of elastic area ($F_s^m > 0$ and/or $F_s^m > 0$) into two distinct subdomains: $\boldsymbol{\mathcal{D}_1}$ and $\boldsymbol{\mathcal{D}_2}$. In subdomain $\boldsymbol{\mathcal{D}_2}$ (respectively subdomain $\boldsymbol{\mathcal{D}_1}$), projection will be performed by using F_s^m and G_s^m (respectively F_t^m and G_t^m) and their associated partial derivatives for shear failure (respectively tensile failure). It is also the same procedure for the weakness planes.

Table 1 Recapitulation of fractures zone extension around drifts in URL (Armand et al. 2014)

$N65//\sigma_h$	In situ observations (after Armand et al. 2014)							
	Extensional fractures extent			Shear fractures extent			ZFC	ZFD
	Min	Average	Max	Min	Average	Max	extent	extent
Roof	0.2xD	0.3xD	0.4xD	0.5xD	0.6xD	0.8xD	0.4xD	0.8xD
Sides	0.1xD	0.1xD	0.2xD	-	-	-	0.2xD	0.6xD
Floor	0.2xD	0.4xD	0.5xD	0.8xD	0.8xD	1.1xD	0.5xD	1.1xD
$N155//\sigma_H$	In situ observations (after Armand et al. 2014)							
	Extensional fractures extent			Shear fractures extent			ZFC	ZFD
	Min	Average	Max	Min	Average	Max	extent	extent
Roof	-	0.1xD	0.15xD	-	-	-	0.15xD	0.5xD
Sides	0.01xD	0.2xD	0.4xD	0.7xD	0.8xD	1xD	0.4xD	1.0xD
Floor	-	0.1xD	0.15xD	-	-	-	0.15xD	0.5xD

Table 2 Values of input parameters (lower bound)

Parameter	Value	Parameter	Value	Parameter	Value	Parameter	Value
$E_1=E_s$	5.6 GPa	m_i	1.5	m_p	2	σ_3^{bd}	25 MPa
$E_3=E_n$	4 GPa	s_i	1	s_p	0.128	s_r	0
$G_{13}=G_{sn}$	[a]	σ_{ci}	9.6 MPa	σ_{cp}	33.5 MPa	m_r(output)	2.172
$\nu_{12}=\nu_{st}$	0.3	C_{wp}	0.9 MPa	φ_{wp}	37°	γ^{peak}	$5.75\ 10^{-3}$
$\nu_{13}=\nu_{sn}$	0.25	σ_t^{wp}	0.125 MPa	ψ_{wp}	0°	γ^{res}	$15.5\ 10^{-3}$
β_0	-0.1	β_m	0.3	b_β	600	γ^{ult}	$16.5\ 10^{-3}$

[a] G_{13}=1806.5 MPa is estimated based on the empirical relationship proposed by Lekhnitski (1981)

Table 3 Predicted plastic zones around GCS drift and their correlation with the ZFD and ZFC zones

$N155//\sigma_H$	Numerical predictions							
	Extent of fractured and failed zones			Extent of pre-peak plastic zones			ZFC	ZFD
	Min	Average	Max	Min	Average	Max	extent	extent
Roof	0.02xD	0.02xD	0.04xD	0.3xD	0.3xD	0.3xD	0.04xD	0.3xD
Sides	0.06xD	0.14xD	0.19xD	0.4xD	0.4xD	0.4xD	0.2xD	0.4xD
Floor	0.02xD	0.03xD	0.04xD	0.3xD	0.3xD	0.3xD	0.04xD	0.3xD

Table 4 Predicted plastic zones around GED drift and their correlation with the ZFD and ZFC zones

N65//σ_h	Numerical predictions of extension / diameter							
	Extent of fractured and failed zones			Extent of pre-peak plastic zones			ZFC	ZFD
	Min	Average	Max	Min	Average	Max	extent	extent
Roof	0.3xD	0.3xD	0.3xD	0.5xD	0.5xD	0.6xD	0.3xD	0.6xD
Sides	-	0.01xD	0.02xD	0.2xD	0.3xD	0.3xD	0.02xD	0.3xD
Floor	0.2xD	0.2xD	0.3xD	0.6xD	0.6xD	0.6xD	0.3xD	0.6xD

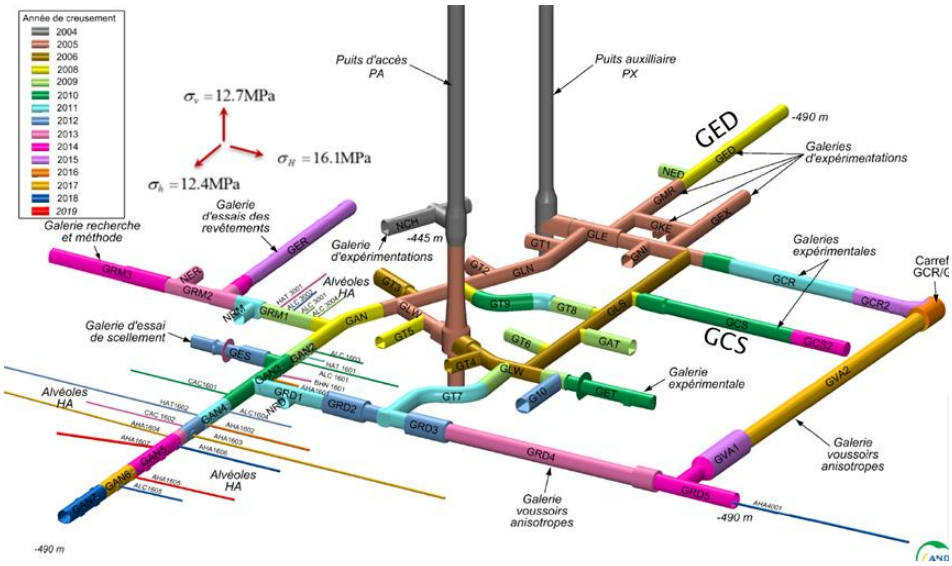

Fig.1: Meuse/Haute-Marne URL drifts network (colour per year)

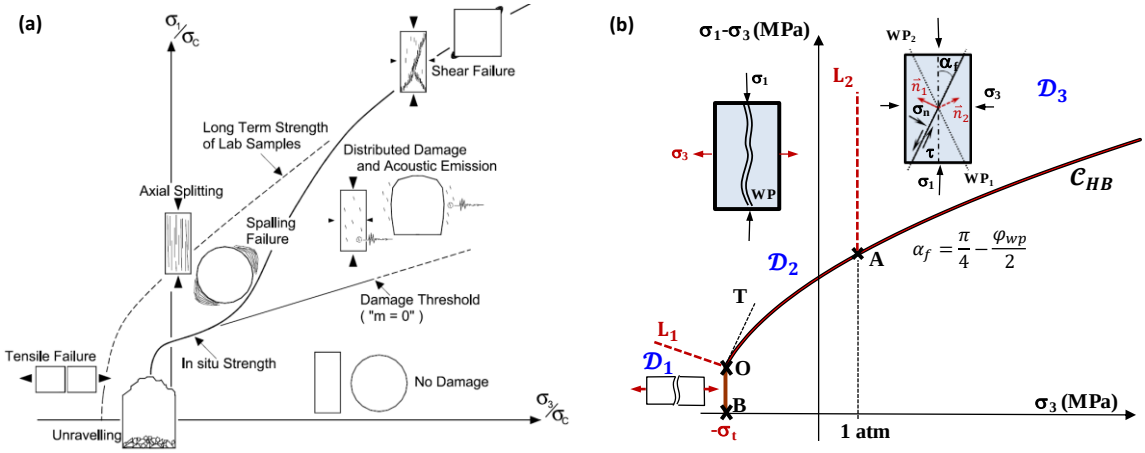

Fig. 2: Schematic of failure envelopes for distinct rock mass failure mechanisms: (a) synthesis after Diederichs (2003), (b) weakness plane failure envelope and orientation adopted in the proposed model (definitions are reported in Appendix A)

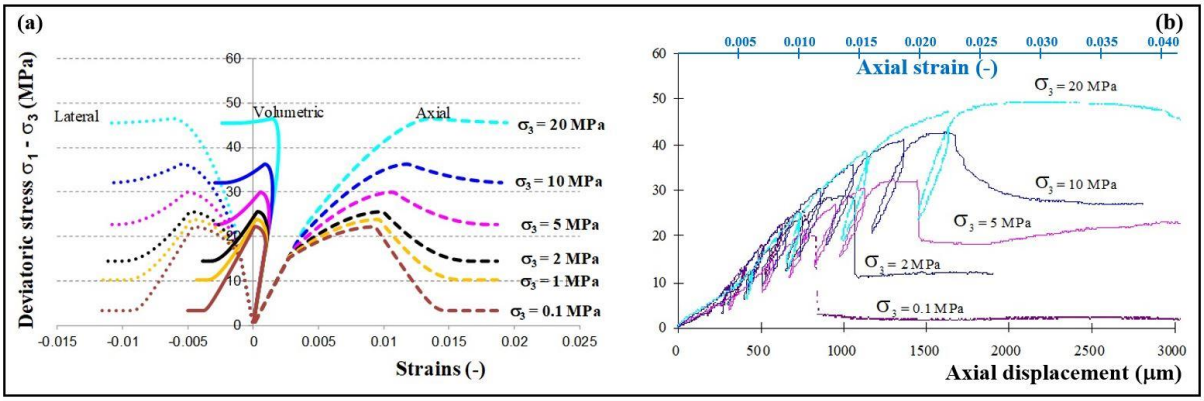

Fig. 3: Triaxial compression tests: (a) numerical simulations, deviatoric stress vs strains; (b) laboratory tests, deviatoric stress vs axial displacement (axial strain axis was added: values of strains were back-calculated by dividing the axial displacement measured with the external inter-plateau sensors and the average sample height of 75.6 mm)

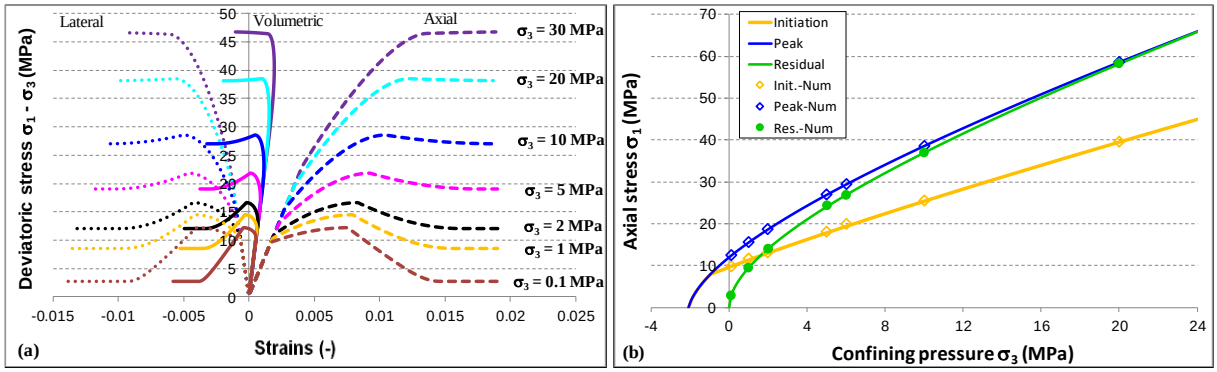

Fig. 4: Numerical verification and validation – single matrix: (a) triaxial compression simulations, (b) elastic limit, peak and residual strengths: numerical and theoretical solutions

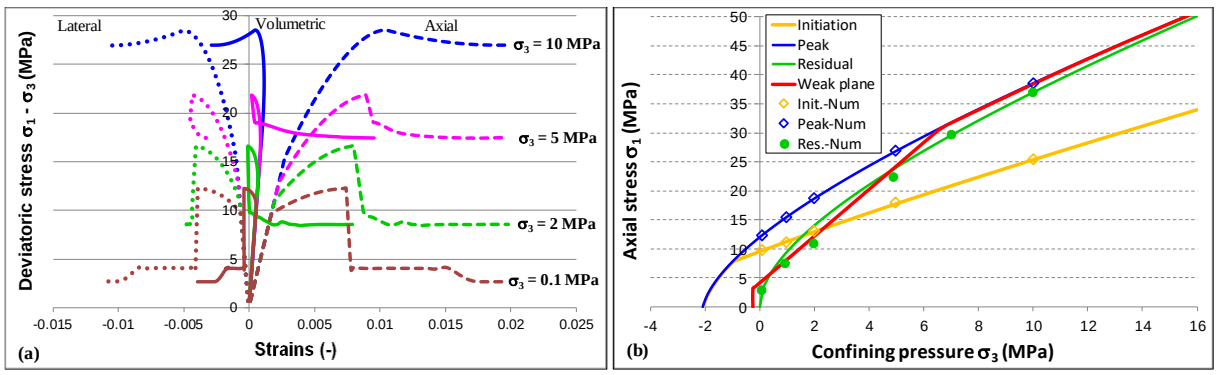

Fig. 5: Numerical verification and validation – both matrix and weakness planes: (a) triaxial compression simulations, (b) elastic limit, peak and residual strengths: numerical and theoretical solutions

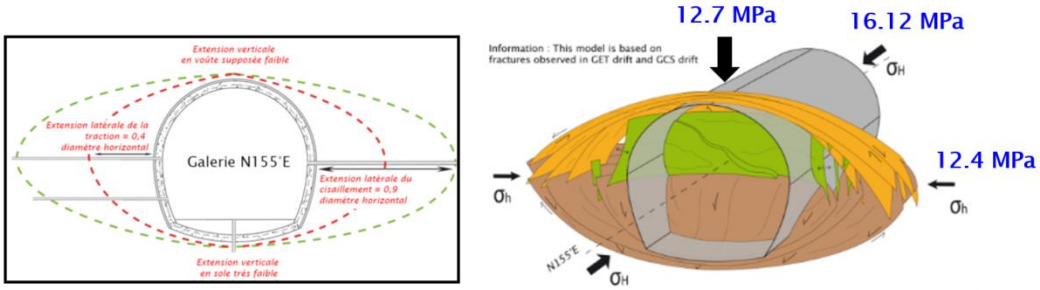

Fig. 6: Conceptual model of EFZ for drifts // σ_H (Armand et al. 2014)

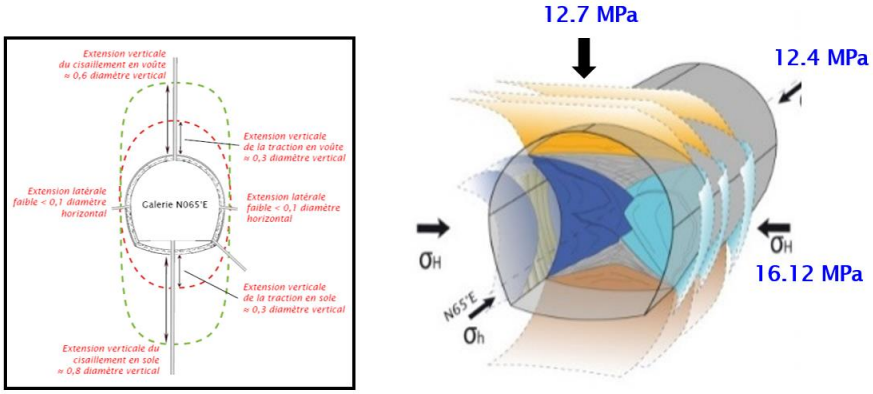

Fig. 7: Conceptual model of EFZ for drifts // σ_h (Armand et al. 2014)

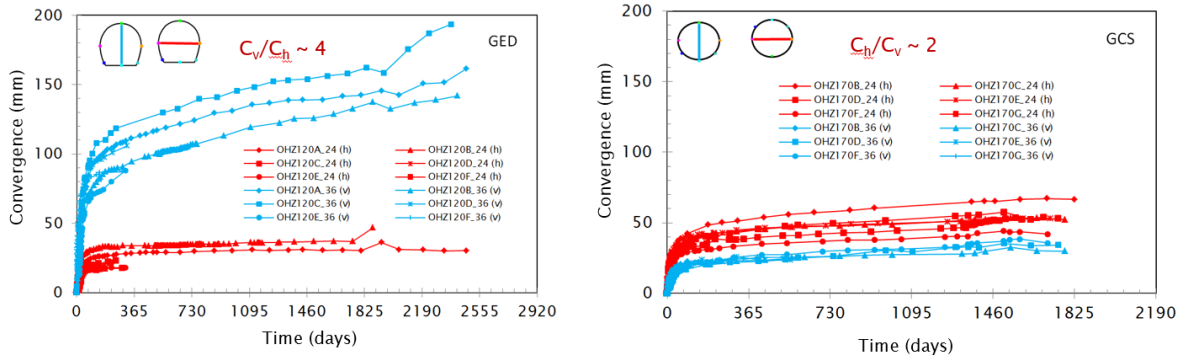

Fig. 8: Measured convergences of GED (//σ_h) and GCS (//σ_H) drifts

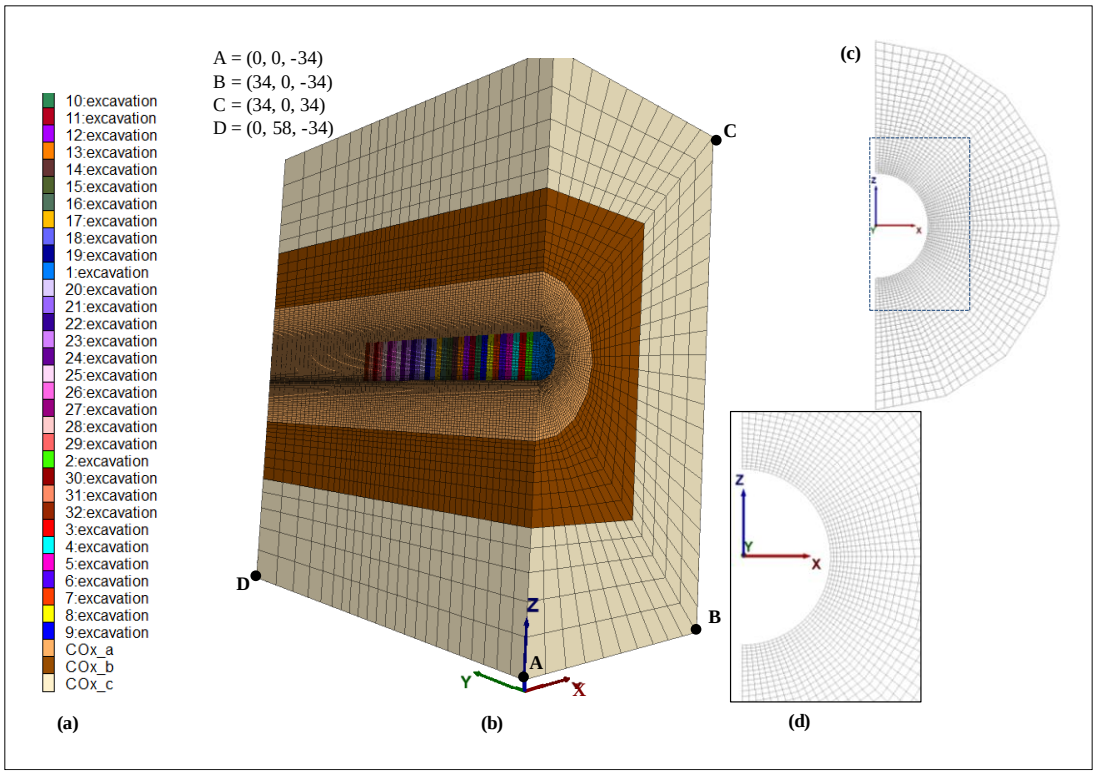

Fig. 9: Geometry and mesh for modelling GCS and GED drifts: (a) 32 steps of drifts excavation and surrounding groups, (b) mesh size, (c) cross-section of group COx_a surrounding the drifts (cylinder with inner radius of 2.6 m and outer radius of 5.2 m), (d) zoom of mesh in COx_a

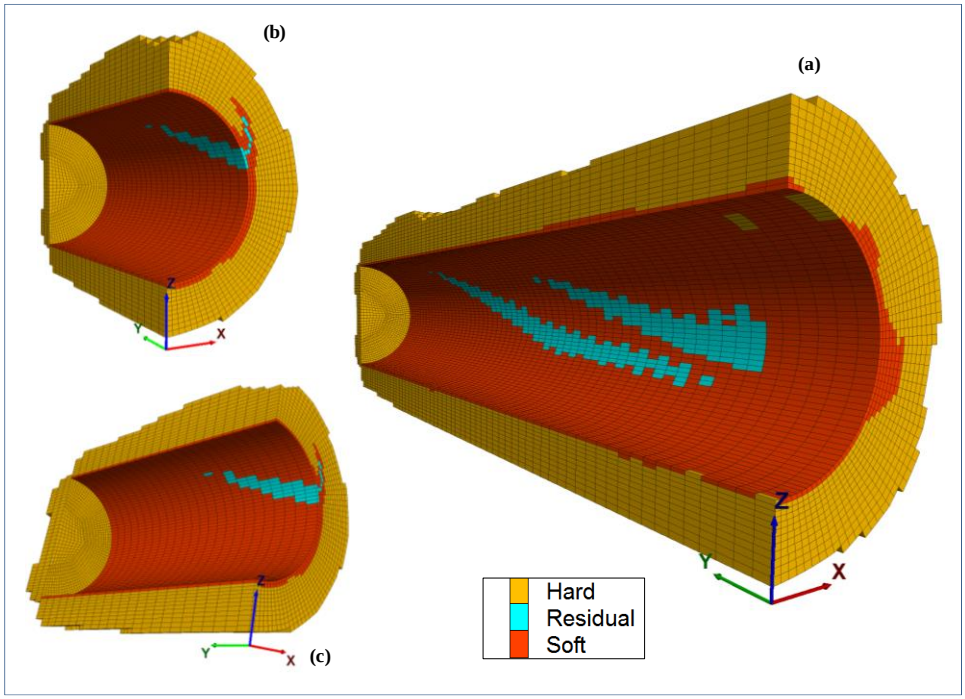

Fig. 10: Predicted extent of plastic zones around the GCS drift: (a) full 32m of excavation; (b)-(c) view of the last 12m of excavation

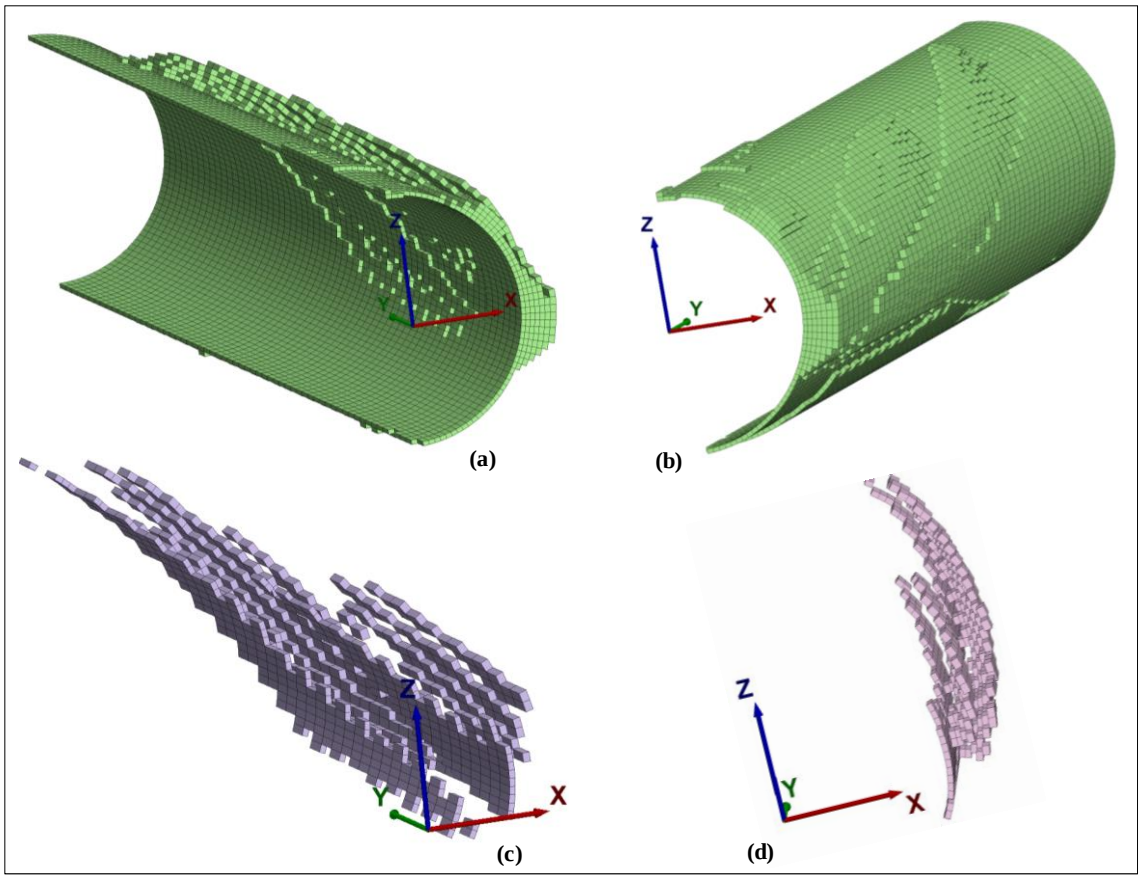

Fig. 11: Predicted extent of failed (associated to post-peak behaviour) zones around GCS: (a) and (b) zone with strain softening behaviour (Soft state); (c) and (d) zones in residual phase

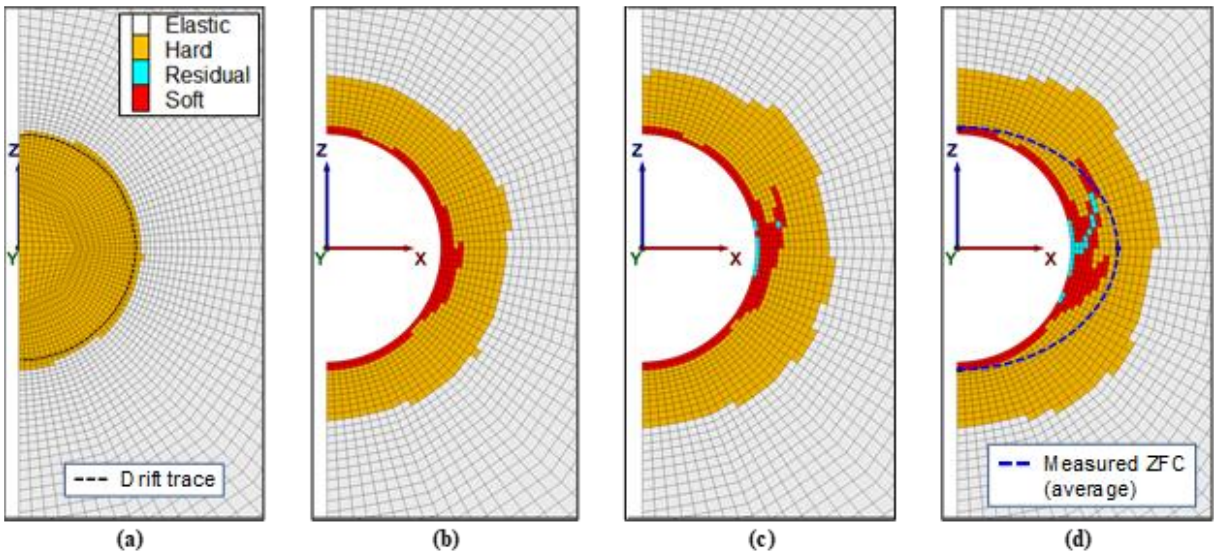

Fig. 12: Extension of plastic zones around section GCS1 (located at 5.5 m). Excavation face at: (a) the section position; (b) 5.5 m (~1 D) after section GCS1; (c) 10.5 m (~2 D) after section GCS1; (d) 26.5 m (~5 D) after section GCS1 or end of the excavation

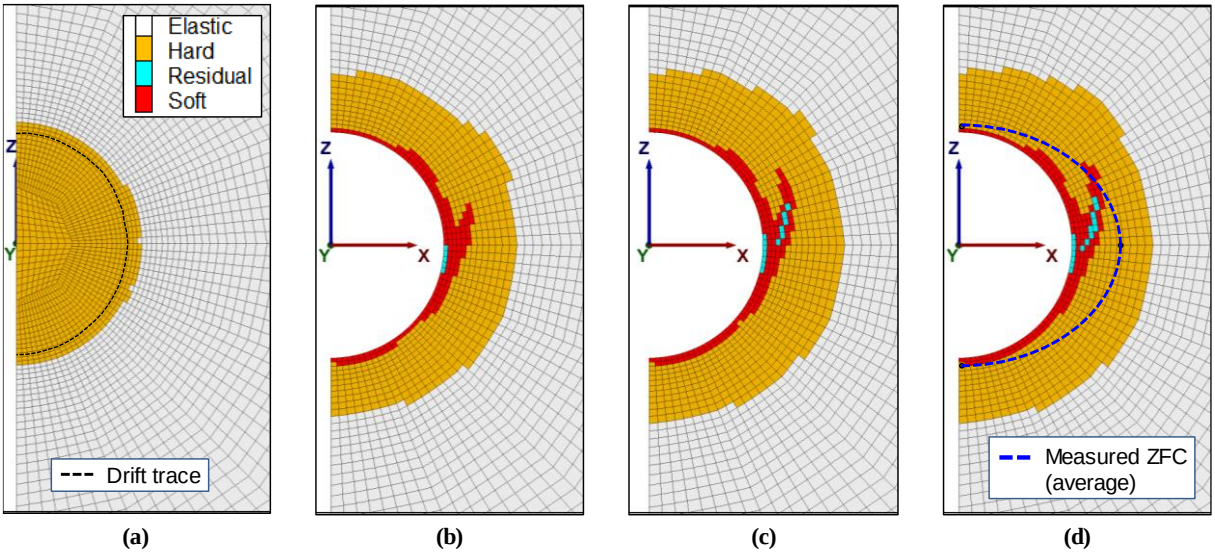

Fig. 13: Extension of plastic zones around section GCS3 (located at 15.5 m). Excavation face at: (a) the section position; (b) 5.5 m (~1 D) after section GCS3; (c) 10.5 m (~2 D) after section GCS3; (d) 16.5 m (~3 D) after section GCS3 or end of the excavation

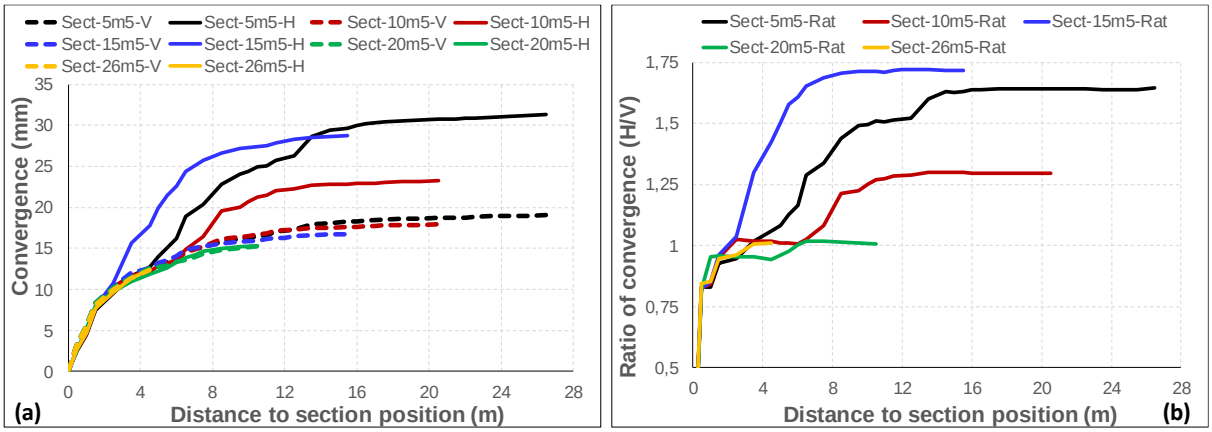

Fig. 14: Results of numerical simulations - (a) Magnitude of horizontal and vertical convergences and (b) ratio of convergences with respect to the face advance for several cross section positions (5.5, 10.5, 15.5, 20.5 and 26.5 m) of GCS drift

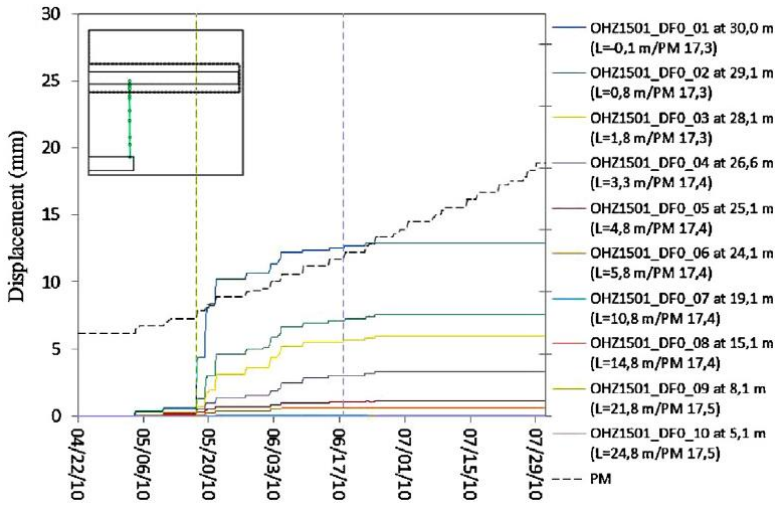

Fig. 15: Radial displacement in the ground around GCS drift during the short term response (Armand et al. 2013)

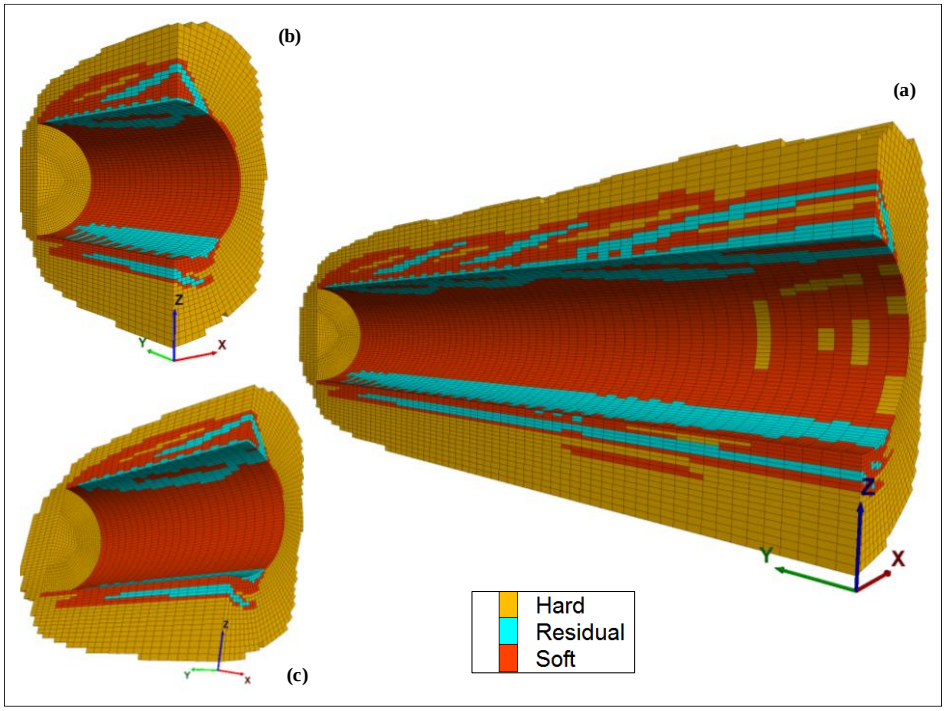

Fig. 16: Predicted extent of plastic zones around the GED drift: (a) full 32 m of excavation; (b)-(c) the last 12m of excavation

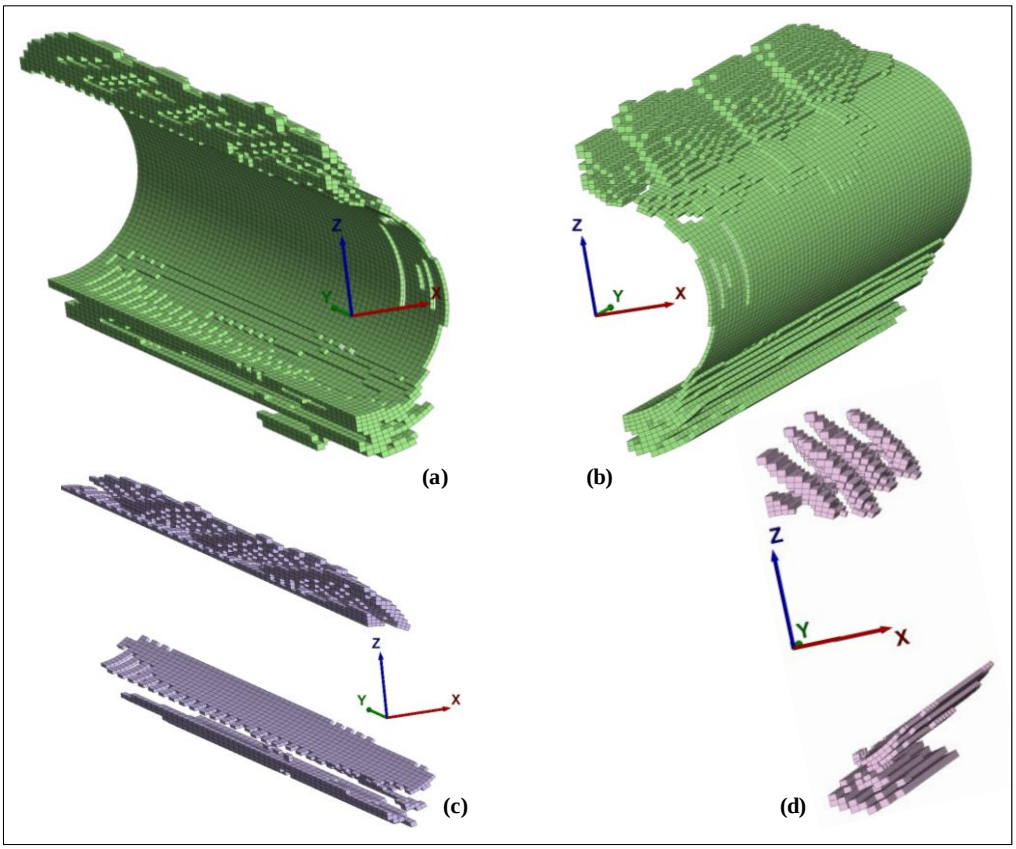

Fig. 17: Predicted extent of failed (associated to post-peak behaviour) zones around GED: (a) and (b) zone with strain softening behaviour (Soft zones); (c) and (d) zones in residual phase

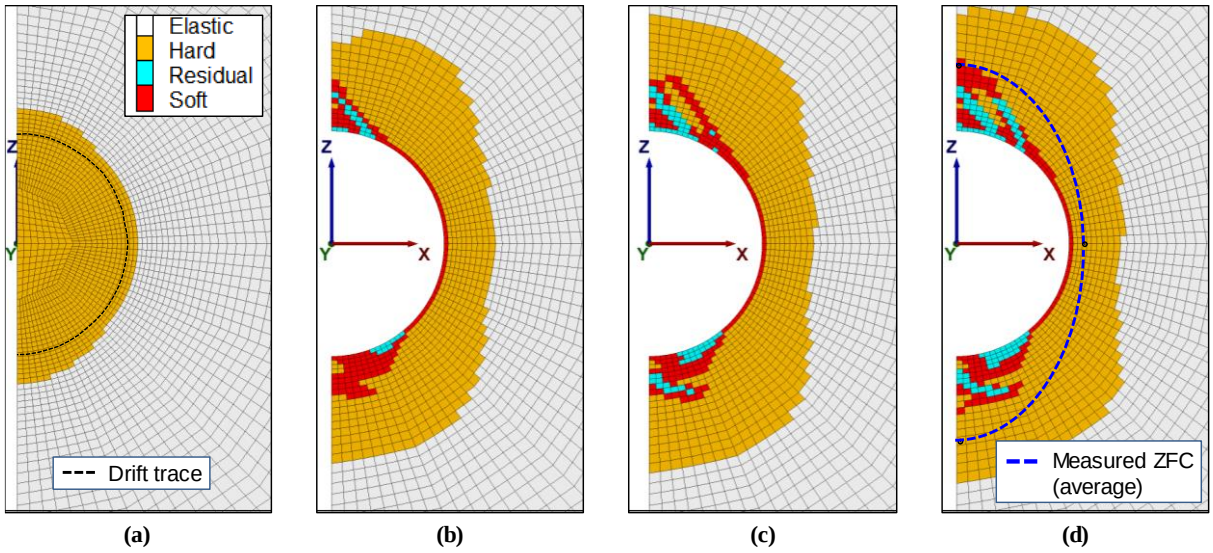

Fig. 18: Extension of plastic zones around section GED1 (l = 5.5 m). Excavation face at: (a) h = 0; (b) h = 5.5 m (~1 D); (c) h = 10.5 m (~2 D); (d) h = 26.5 m (~5 D) or end of the excavation

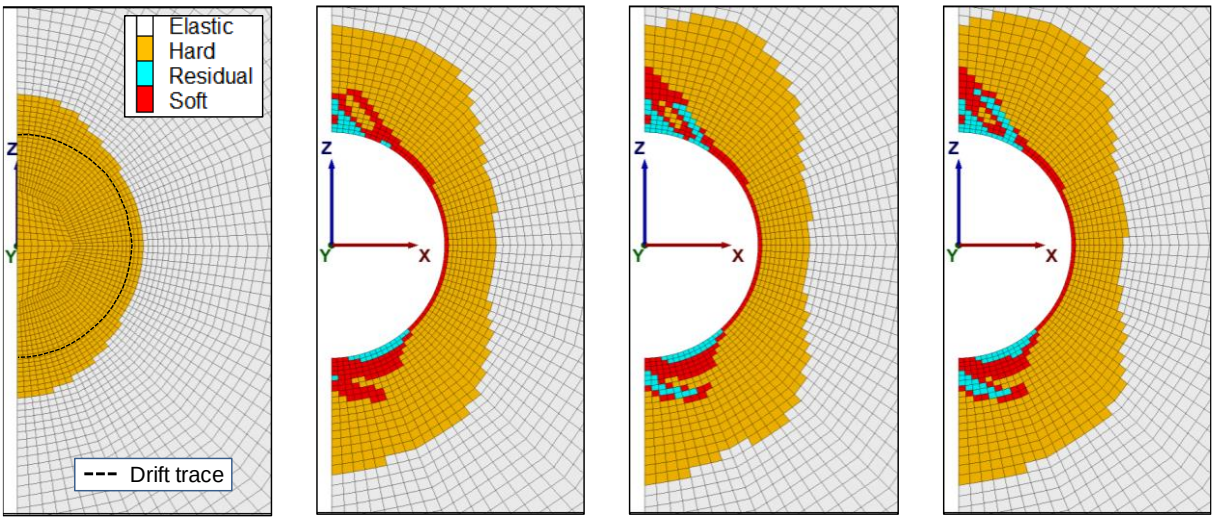

Fig. 19: Extension of plastic zones around section GED3 (l = 15.5 m). Excavation face at: (a) position = 0; (b) h = 5.5 m (~1 D); (c) h = 10.5 m (~2xD); (d) h = 16.5 m (~3 D) or end of the excavation

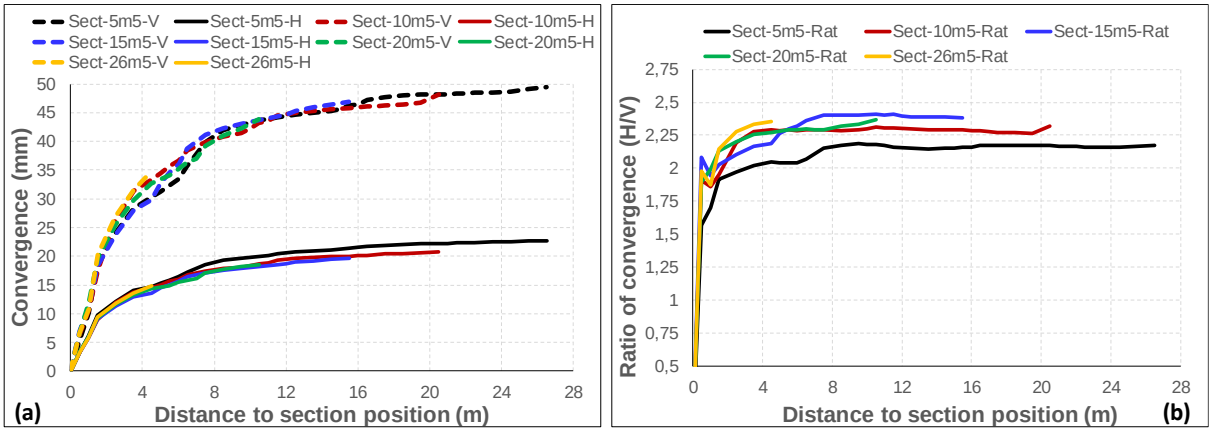

Fig. 20: Results of numerical simulations - Horizontal and vertical convergences (a) and ratio of convergences (b) with respect to the face advance for several cross section positions (l = 5.5, 10.5, 15.5, 20.5 and 26.5 m) of GED drift